J Comput Neurosci (2014) 36:259–278
DOI 10.1007/s10827-013-0470-8

A geometric understanding of how fast activating potassium channels promote bursting in pituitary cells

Theodore Vo · Joël Tabak · Richard Bertram · Martin Wechselberger

Received: 12 February 2013 / Revised: 25 April 2013 / Accepted: 29 May 2013 / Published online: 3 July 2013

Abstract The electrical activity of endocrine pituitary cells is mediated by a plethora of ionic currents and establishing the role of a single channel type is difficult. Experimental observations have shown however that fast-activating voltage- and calcium-dependent potassium (BK) current tends to promote bursting in pituitary cells. This burst promoting effect requires fast activation of the BK current, otherwise it is inhibitory to bursting. In this work, we analyze a pituitary cell model in order to answer the question of why the BK activation must be fast to promote bursting. We also examine how the interplay between the activation rate and conductance of the BK current shapes the bursting activity. We use the multiple timescale structure of the model to our advantage and employ geometric singular perturbation theory to demonstrate the origin of the bursting behaviour. In particular, we show that the bursting can arise from either canard dynamics or slow passage through a dynamic Hopf bifurcation. We then compare our theoretical predictions with experimental data using the dynamic clamp technique and find that the data is consistent with a burst mechanism due to a slow passage through a Hopf.

Keywords Bursting · BK channel · Mixed mode oscillations · Geometric singular perturbation theory · Dynamic clamp

Action Editor: David Terman

T. Vo (✉) · M. Wechselberger
School of Mathematics and Statistics,
University of Sydney, Sydney, NSW, Australia
e-mail: theodore.vo@sydney.edu.au

J. Tabak
Department of Mathematics, Florida State University,
Tallahassee, FL, USA

R. Bertram
Department of Mathematics and Programs in Neuroscience
and Molecular Biophysics, Florida State University,
Tallahassee, FL, USA

1 Introduction

The electrical activity of pituitary cells regulates diverse functional characteristics such as the release of prolactin, growth hormone and ACTH in lactotrophs, somatotrophs and corticotrophs, respectively. The combination of ionic currents mediated by various ion channels in the cellular membrane determines the pattern of electrical activity exhibited by these cells (Stojilkovic et al. 2010). One particular pattern of electrical activity commonly seen in pituitary cells is *pseudo-plateau bursting* (Stern et al. 2008), which consists of alternating periods of small-amplitude oscillations in the active (depolarized) phase followed by silent phases (Fig. 1a). The calcium concentration in these cells increases more when the cell is bursting than when it is spiking, resulting in higher levels of hormone and neurotransmitter secretion (Stojilkovic et al. 2005; Van Goor et al. 2001). We distinguish pseudo-plateau bursting from plateau bursting, which features large-amplitude fast spiking in the active phase (Bertram et al. 1995; LeBeau et al. 1998; Tsaneva-Atanasova et al. 2007). The bursting type we examine in this paper is the pseudo-plateau type.

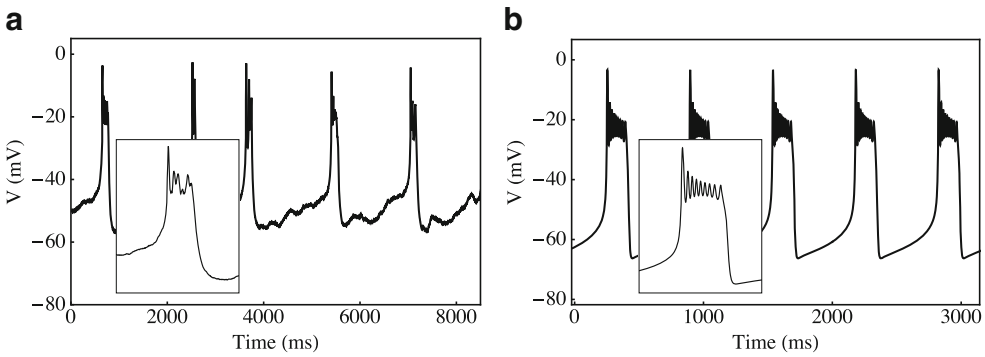

Fig. 1 Electrical activity of pituitary cells. **a** Pseudo-plateau bursting recorded in an unstimulated GH4C1 lacto-somatotroph cell line and **b** MMOs generated by a deterministic mathematical model. Insets: magnified view of a single burst with sub-threshold oscillations in the active phase

Pituitary cells express a variety of ion channels and establishing the role of any given channel type remains a significant undertaking. It has been proposed that large conductance potassium (BK) channels (Latorre and Brauchi 2006; Sah and Faber 2002; Stojilkovic et al. 2010) primarily determine whether a pituitary cell spikes or bursts (Miranda et al. 2003; Stojilkovic et al. 2005). In Tabak et al. (2011), a hybrid computational/experimental approach was used to study how the kinetic properties of BK channels affect bursting in pituitary cells. It was demonstrated that subtracting/adding BK current tended to decrease/increase burstiness. Blocking of the BK channels using paxilline or iberiotoxin generally resulted in an irreversible conversion from bursting to spiking. Using the dynamic clamp technique (Sharp et al. 1993), artificial BK current was then injected into the cell, which was observed to reliably return the cell to a bursting state. Moreover, increasing the conductance of the injected BK current also increased burst duration. However, it was also observed that the burst promoting effect of the BK current came with a caveat: BK activation must be sufficiently fast to promote bursting. If the BK activation is too slow, then the BK current becomes inhibitory to bursting by speeding up repolarization (Tabak et al. 2011). The primary aim of this work is to provide a mathematical explanation of the key physiological observations of Tabak et al. (2011). Namely, to understand why increasing BK conductance promotes bursting and why BK activation must also be fast in order to promote bursting.

The dependence of the electrical activity on the activation rate of the BK channels highlights the importance of timescales in cellular excitability. Experimental recordings and model simulations of pituitary cell bursting support this notion by showing that the dynamics evolve on multiple timescales. There are fast epochs where the cell switches between active and silent phases and slow epochs where the sub-threshold oscillations of the bursting can occur. Using geometric singular perturbation theory (GSPT) (Fenichel 1979; Jones 1995), it has been shown that the pseudo-plateau bursting is a mixed mode oscillation (MMO) (Vo et al. 2010; Teka et al. 2011). A MMO is an oscillatory trajectory featuring small amplitude oscillations sitting on top of large amplitude, relaxation-type oscillations (Fig. 1b). Two common mechanisms for MMOs are canard dynamics and slow passage through a dynamic Hopf bifurcation (Brøns et al. 2008; Desroches et al. 2012; Erchova and McGonigle 2008; Izhikevich 2000). In the current article, we analyze a pituitary cell model and show that both canard and Hopf mechanisms are possible, depending on parameter values.

The outline of the paper is as follows: in Section 2, we describe the mathematical model and perform a bifurcation analysis with respect to kinetic properties of the BK current. We show numerically that BK conductance and BK activation rate alone are insufficient to control bursting. Instead, it is a combination of the BK conductance and BK activation rate that controls the bursting behaviour. In Section 3 we formally show that our model is a multiple timescale problem and give a brief overview of GSPT in the context of our bursting model. In Section 4, we use our geometric singular perturbation analysis to explain, mathematically, the bursting behaviour encountered in Section 2 via canard- and Hopf-induced MMOs. In particular, we demonstrate that both MMO mechanisms are affected by the BK conductance, however, only the Hopf mechanism generates MMOs that depend on the BK activation rate. That is, we show that sensitivity to variations in the BK activation rate is an useful diagnostic in identifying the burst mechanism. In Section 5, we test our geometric analysis experimentally by injecting artificial BK conductance into spiking GH4 cells (a lacto-somatotroph cell line) using the dynamic clamp technique. As we decrease the activation time constant of BK channels, we observe longer bursts with smaller sub-threshold oscillations during the active phase, consistent with the Hopf mechanism. We conclude in Section 6 with a discussion.

2 The mathematical model

We consider a mathematical model that provides a minimal description of the electrical activity and calcium dynamics in pituitary cells (Tabak et al. 2011). There are three

voltage-gated currents (I_{Ca}, I_{BK}, I_K), a calcium-gated current, I_{SK}, and a leak current, I_L. The voltage-gated inward calcium current I_{Ca} is assumed to activate instantaneously (so that the activation variable is fixed at its quasi steady state). Despite being gated by both voltage and calcium, the BK channels are modelled as a purely voltage-dependent process since the calcium concentration felt by the BK channels is determined by the voltage-dependent current through a nearby calcium channel and equilibrates in microseconds (Fakler and Adelman 2008; Sherman et al. 1990). The state variables are the membrane potential V of the cell, activation variables n and b for the K and BK channels, respectively, and the intracellular calcium concentration c. Their dynamics are governed by the evolution equations

$$\begin{aligned} C_m \frac{dV}{dt} &= -(I_{Ca} + I_{BK} + I_K + I_{SK} + I_L), \\ \tau_{BK} \frac{db}{dt} &= b_\infty(V) - b, \\ \tau_n \frac{dn}{dt} &= n_\infty(V) - n, \\ \frac{dc}{dt} &= -f_c(\alpha I_{Ca} + k_c c), \end{aligned} \tag{1}$$

where the ionic currents are given by

$$\begin{aligned} I_{Ca} &= g_{Ca} m_\infty(V)(V - V_{Ca}), \\ I_{BK} &= g_{BK} b (V - V_K), \\ I_K &= g_K n (V - V_K), \\ I_{SK} &= g_{SK} s_\infty(c)(V - V_K), \\ I_L &= g_L (V - V_L), \end{aligned} \tag{2}$$

and the steady state functions are given by

$$\begin{aligned} x_\infty(V) &= \left[1 + \exp\left(\frac{V_x - V}{s_x}\right)\right]^{-1}, \\ s_\infty(c) &= \frac{c^2}{c^2 + k_s^2}, \end{aligned}$$

where $x \in \{m, b, n\}$. Standard parameter values are listed in Table 1.

Table 1 Standard parameter values for the 4D pituitary cell model

Parameter	Value	Definition
C_m	$0 - 10$ pF	Membrane capacitance
g_{Ca}	2 nS	Maximal conductance of Ca^{2+} channels
V_{Ca}	60 mV	Reversal potential for Ca^{2+}
V_m	−20 mV	Voltage value at midpoint of m_∞
s_m	12 mV	Slope parameter of m_∞
g_K	1.5 nS	Maximal conductance of delayed rectifier K^+ channels
V_K	−75 mV	Reversal potential for K^+
V_n	−5 mV	Voltage value at midpoint of n_∞
s_n	10 mV	Slope parameter of n_∞
τ_n	30 ms	Time constant of n
g_{SK}	2 nS	Maximal conductance of SK channels
k_s	0.4 μM	Ca^{2+} at midpoint of s_∞
g_{BK}	$0 - 1$ nS	Maximal conductance of BK channels
V_b	−20 mV	Voltage value at midpoint of b_∞
s_b	2 mV	Slope parameter of b_∞
τ_{BK}	$2 - 10$ ms	Time constant of b
g_L	0.2 nS	Leak conductance
V_L	−50 mV	Leak current reversal potential
f_c	0.01	Fraction of free Ca^{2+} ions in cytoplasm
α	0.0015 μMfC^{-1}	Conversion from charges to molar concentration
k_c	0.12 ms^{-1}	Rate of Ca^{2+} extrusion

2.1 Fast-activating BK channels promote bursting

One of the key observations from Tabak et al. (2011) was that the activation of the BK channels needed to be fast in order to promote bursting. Otherwise, the BK current has an inhibitory effect and the cell spikes. A systematic way to investigate the dependence of the speed of activation on the bursting in Eq. (1) is via a bifurcation analysis. That is, examining what happens to the system dynamics under variations in the activation time constant.

In Fig. 2a–f, representative time traces for different types of bursts are shown for a fixed value of g_{BK}. For large τ_{BK} (i.e. slow activation), the BK current hinders the bursting and the system is in a spiking state (panel (a)). When the activation time constant is decreased, the system generates bursts (panels (b)–(d)). These bursts have sensitive dependence to τ_{BK}. Speeding up the activation of the BK channels (i.e. making τ_{BK} smaller) rapidly increases the number of small oscillations in the bursts. Moreover, as τ_{BK} decreases, so too does the amplitude of the small oscillations in the burst. For sufficiently small τ_{BK}, we observe damped oscillations followed by a plateau in the active phase before the trajectory jumps away to the silent phase (panel (e)). Further decreases in τ_{BK} only intensify the damping effect and the oscillatory behaviour gives way to a flat plateau (panel (f)). Henceforth, we explicitly distinguish between bursting (panels (b)–(d)) and plateau oscillations (panels (e) and (f)).

A graphical summary of the effect of τ_{BK} variations on the trajectories is provided in panel (g), where the bifurcation structure of Eq. (1) with respect to τ_{BK} for $C_m = 5$ pF and $g_{BK} = 0.5$ nS was computed using AUTO (Doedel 1981; Doedel et al. 2009). We plot τ_{BK} against the standard

Euclidean norm of the solution. As τ_{BK} is decreased, the behaviour switches from spiking to bursting with increasing duration, to plateauing. Distinct bursting families are distinguished by the number, s, of small oscillations in the active phase. The spiking branch (blue, labelled $s = 0$) is stable for the largest τ_{BK} values. The stability changes at a period doubling (PD) bifurcation (PD_1, right inset) and the $s = 1$ bursting family becomes stable at a saddle-node (SN) of periodics (SN_1, right inset). Between the spiking and first bursting branch is a small τ_{BK} interval where the trajectory is a mixture of spiking and bursting patterns. This behaviour of stability loss at a PD and stabilization at a SN with mixed bursting trajectories in between persists for the remaining bursting transitions, except for the transition between the $s = 6$ bursting branch and the plateau branch (left inset). In this case there are no bifurcations separating the two branches. That is, from a dynamical systems viewpoint, there is no intrinsic difference between the last bursting family and a plateau trajectory.

The time traces in Fig. 2 show that the amplitude and number of small oscillations in the bursts changes very rapidly under τ_{BK} variations when all other parameters are fixed. However, changes in the other system parameters alter the bifurcation structure and hence the associated time traces. Figure 3e shows an example of how a change in g_{BK} for instance, can have a drastic impact on the bifurcation structure of Eq. (1). Note that the L_2 norm has a much smaller vertical range than its counterpart in Fig. 2g. The relatively flat L_2 norm depicted in Fig. 3e is reflected in the trajectories (panels (a) to (d)) as a weak response to τ_{BK} variations. That is, the number and amplitude of the sub-threshold oscillations in the bursting patterns has little variation under τ_{BK} variations. Moreover, the burst duration is essentially unaltered.

2.2 The interplay between BK conductance and activation speed

In the dynamic clamp studies conducted in Tabak et al. (2011), artificial BK current was injected into pituitary cells not only for different activation rates τ_{BK}, but also for various conductances g_{BK}. In Section 2.1, we investigated the dependence of the bursts on the activation time constant for two different fixed g_{BK} values. Figures 2 and 3 hinted at the notion that (in addition to τ_{BK}) g_{BK} is a crucial factor in shaping the electrical activity. We now extend that analysis and examine the dependence of the bursts on both the amount of BK current and its speed of activation. To do this, we compute 2-parameter bifurcation diagrams in (τ_{BK}, g_{BK})-space (Fig. 4).

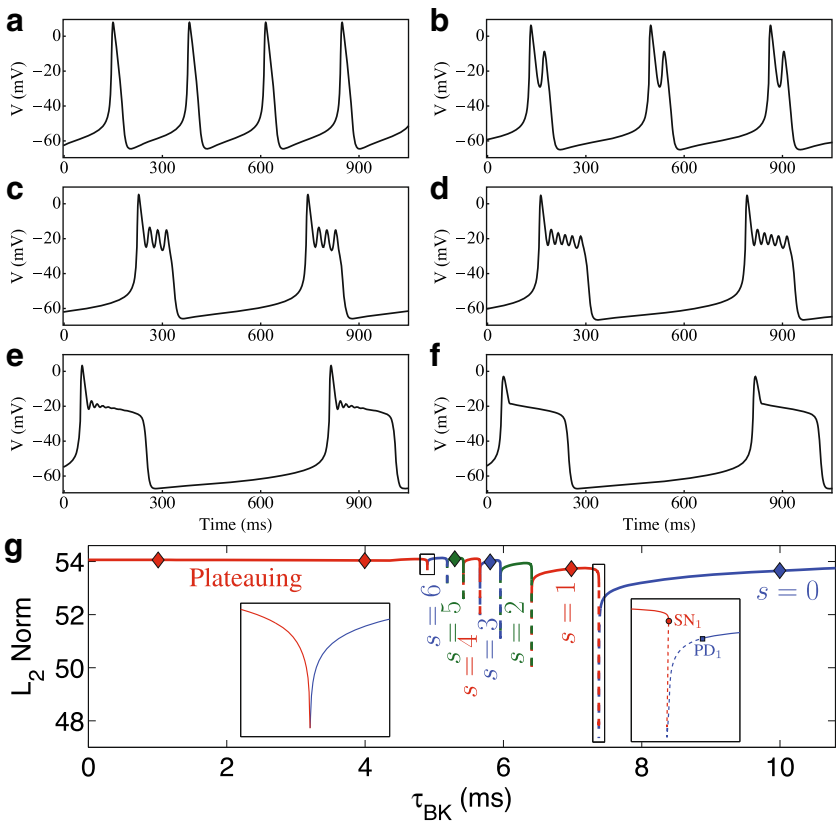

Fig. 2 Effect of variations in τ_{BK} on the trajectories of Eq. (1) for $C_m = 5$ pF and $g_{BK} = 0.5$ nS with all other parameters fixed at their standard values. In **a** $\tau_{BK} = 10$ ms (spiking), **b** $\tau_{BK} = 7$ ms (bursting with 1 small oscillation), **c** $\tau_{BK} = 5.8$ ms (bursting with 3 small oscillations), **d** $\tau_{BK} = 5.3$ ms (bursting with 5 small oscillations), **e** $\tau_{BK} = 4$ ms (plateauing with visibly damped oscillations) and **f** $\tau_{BK} = 1$ ms (plateauing with no observable oscillations). **g** Summary of all possible behaviours as τ_{BK} is varied

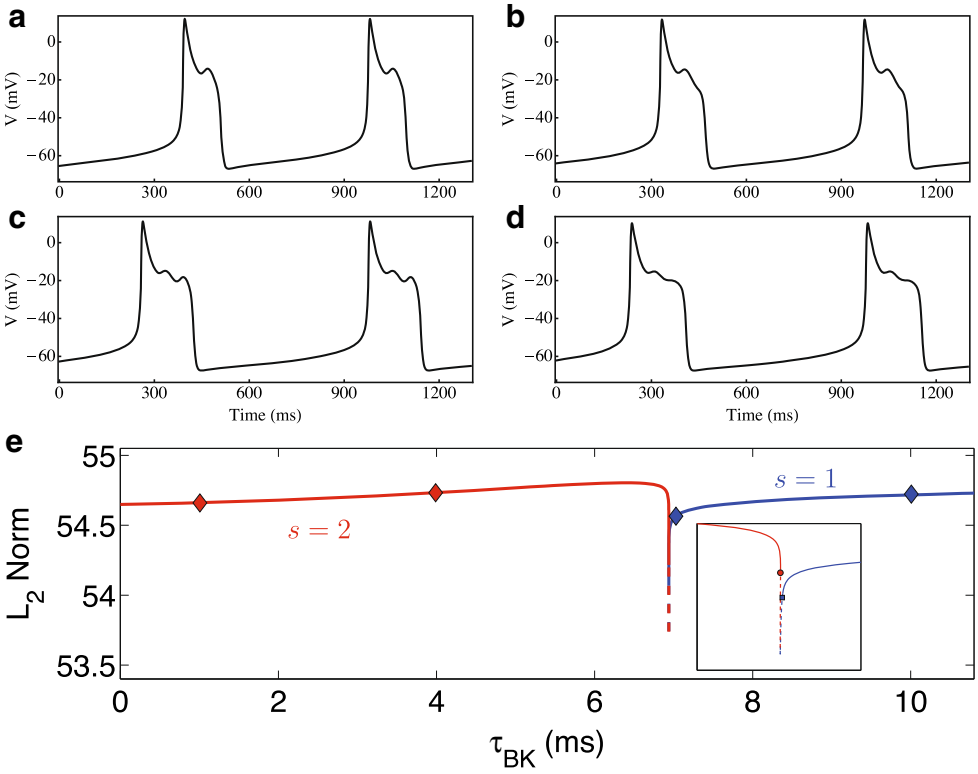

Fig. 3 Time traces and bifurcation structure of Eq. (1) for $C_m = 5$ pF and $g_{BK} = 0.1$ nS with other parameters as given in Table 1. In **a**, $\tau_{BK} = 10$ ms, **b** $\tau_{BK} = 7$ ms, **c** $\tau_{BK} = 4$ ms and **d** $\tau_{BK} = 1$ ms. Variations in the activation rate τ_{BK} only creates minor changes in the bursting patterns. The bifurcation diagram in panel **e** illustrates the notion that τ_{BK} has little influence on the bursting trajectories for this particular parameter set

In Fig. 4a, the spiking/bursting boundary (blue, PD_1) was calculated by following in 2 parameters the PD point where the $s = 0$ branch loses stability. Also shown is the boundary between bursts with 1 small oscillation and more complex trajectories (also computed by following in (τ_{BK}, g_{BK}) the PD point where the $s = 1$ branch becomes unstable)[1]. For this particular parameter set, bursting exists in the absence of BK current. Spiking only occurs when slowly-activated BK current is injected. If the injected BK current is sufficiently fast, then the resulting trajectory is either a burst or a plateau oscillation. Above a certain g_{BK} threshold (approximately given by the nearly horizontal segment of the red boundary), the activation speed of the BK current becomes crucial: small variations in τ_{BK} change the number and amplitude of the small oscillations in the burst pattern significantly. Below the threshold, the bursting trajectories are largely independent of τ_{BK}. That is, large variations in τ_{BK} produce only minor changes in the burst pattern, suggesting that the mechanism that generates the bursts is somehow different above and below the threshold (compare Figs. 2 and 3).

In panel (b), we show the 2-parameter bifurcation structure of Eq. (1) for $C_m = 5$ pF and $g_K = 3.2$ nS. For this given parameter set, the system is calibrated so that in the

[1]We do not draw the bursting/plateau boundary since in AUTO, there seems to be no way of distinguishing between these two types of trajectories.

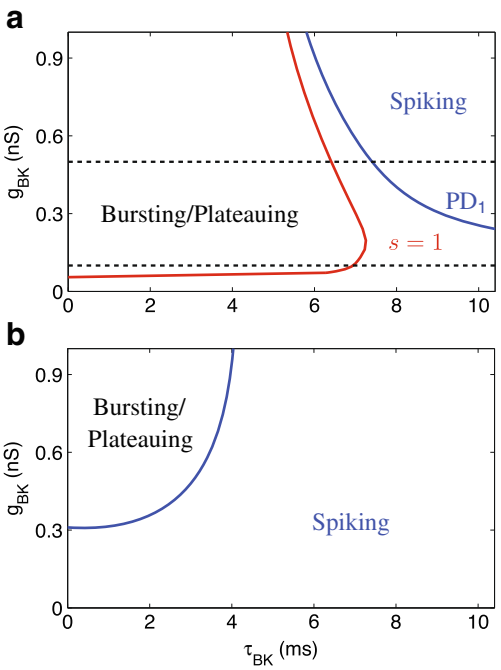

Fig. 4 Spiking/bursting boundaries of Eq. (1) with $C_m = 5$ pF for **a** $g_K = 1.5$ nS and **b** $g_K = 3.2$ nS with all other parameters fixed at their standard values. In (a), bursting exists even in the absence of BK current. In (b), BK current is necessary for bursting. In both cases, the BK current must be activated sufficiently fast, otherwise the system is spiking. The dashed lines in (a) denote the 1D slices taken in Figs. 2g and 3e

absence of BK current it is spiking. The BK current then becomes crucial for bursting. The addition of BK current alone does not guarantee bursting as the activation speed τ_{BK} is a critical factor in determining whether the system spikes or bursts. More specifically, the model predicts that the BK current only produces bursts when τ_{BK} lies in an intermediate τ_{BK} range. If τ_{BK} is too large, then the BK current impedes the burst phenomenon. If it is too small, then the small oscillations in the active phase rapidly die out and only plateau oscillations are observed. Note that the spiking/bursting boundary (blue) has a reversed orientation to its counterpart in panel (a). This orientation flip in the spiking/bursting boundary occurs at $g_K \approx 1.98$ nS and arises from changes in the shape of the PD_1 curve under g_K variations. Despite this, the conclusions are still the same: bursting due to BK current can only occur if the BK activation is sufficiently fast.

So far, we have used bifurcation analysis to partition the parameter space of Eq. (1) based on the dynamical behaviour. Namely, we have identified the regions in (τ_{BK}, g_{BK})-space where the system is spiking and where it is either bursting or plateauing. However, our bifurcation diagrams do not reveal the underlying mechanisms that cause the observed behaviour. In particular, we would like to understand why in some instances τ_{BK} is so crucial in shaping the bursting trajectories whilst in others it has virtually no influence. GSPT forms the basis of our approach.

3 Geometric singular perturbation analysis

Geometric singular perturbation theory (Jones 1995; Rubin and Terman 2002) is an analytic technique for multi-scale problems that combines asymptotic theory with dynamical systems techniques. It has been used to successfully explain the dynamics arising in a variety of biological systems. In the context of bursting, GSPT was pioneered by Rinzel (1985) and has become a very useful tool in understanding burst phenomena (Izhikevich 2007; Ermentrout and Terman 2010). For instance, the classification of bursters is often based on the fast subsystem bifurcations involved in the initiation/termination of the active phase (Bertram et al. 1995; Izhikevich 2000). GSPT has also been used to great effect in unravelling the dynamics of plateau bursting in pancreatic β cells (Bertram and Sherman 2005; Terman 1991), trigeminal motoneurons (Del Negro et al. 1999) and neonatal CA3 hippocampal principal neurons (Safiulina et al. 2008). GSPT is also useful in explaining the relationship between plateau and pseudo-plateau bursting (Osinga and Tsaneva-Atanasova 2010; Teka et al. 2011). The bursting activity of pituitary cells such as cotricotrophs (LeBeau et al. 1998), somatotrophs (Nowacki et al. 2010) and lactotrophs (Teka et al. 2011; Vo et al. 2010) have also been described using GSPT. The examples cited here are far from forming a comprehensive list and are only intended to give a sense of the practical utility of GSPT. Since GSPT relies on the fact that the system evolves on multiple timescales, our first task is to show that system (1) is a multi-timescale problem. By introducing a dimensionless time variable $t = k_t t_s$ and suitable rescalings, we can rewrite Eq. (1) as

$$\begin{aligned}
\varepsilon_1 \frac{dV}{dt_s} = \frac{C_m}{k_t g_{\text{ref}}} \frac{dV}{dt_s} &= f_1(V, b, n, c), \\
\varepsilon_2 \frac{db}{dt_s} = \frac{\tau_{BK}}{k_t} \frac{db}{dt_s} &= b_\infty(V) - b \equiv f_2(V, b), \\
\frac{dn}{dt_s} &= \frac{k_t}{\tau_n}(n_\infty(V) - n) \equiv g_1(V, n), \\
\frac{dc}{dt_s} &= -k_t f_c k_c \left(\frac{\alpha}{k_c} I_{Ca} + c \right) \equiv g_2(V, c),
\end{aligned} \tag{3}$$

where $k_t = \tau_n$ is a reference time scale, $g_{\text{ref}} = \mathcal{O}(1)$ nS is a typical conductance scale and

$$f_1(V, b, n, c) := -\frac{1}{g_{\text{ref}}}(I_{Ca} + I_{BK} + I_K + I_{SK} + I_L).$$

Note that we avoid rescaling of V and c as they have no influence on the timescales. We remark that, strictly speaking, GSPT requires the right hand sides of Eq. (4) to be $\mathcal{O}(1)$, but f_1 is not of the same order as f_2, g_1 or g_2. This is a non-issue since in our calculations, we implicitly assume V has been non-dimensionalized so that $f_1 = \mathcal{O}(1)$ and the ensuing results have been rescaled to restore V to its dimensional form.

From system (4), we can see that the voltage variable has time constant $C_m/g_{\text{ref}} = 1$ ms for $C_m = 5$ pF and $g_{\text{ref}} = 5$ nS. Meanwhile, the activation variable for the BK channels has typical timescale $\tau_{BK} = 5$ ms. The gating variable n is slower with timescale $\tau_n = 30$ ms, whilst the calcium variable is substantially slower with a timescale of $(f_c k_c)^{-1} > 800$ ms. To formalize this timescale separation, we introduce the small parameters $\varepsilon_1 \equiv C_m/(k_t g_{\text{ref}})$ and $\varepsilon_2 \equiv \tau_{BK}/k_t$, which measure the relative speeds of V and b to n, respectively. By decreasing C_m (or ε_1), the timescale separation between V and (b, n, c) increases, whilst decreasing τ_{BK} (or ε_2) changes the timescale separation between b and (V, n, c). Although it is not clear whether or not V and b operate on similar timescales, it is clear that both V and b are substantially faster than (n, c). Thus, system (4) is a singularly perturbed problem with fast variables (V, b), slow variables (n, c) and small perturbation parameters $(\varepsilon_1, \varepsilon_2)$.

System (4) is currently described over the slow timescale t_s. This means that the fast variables (V, b) go through their dynamics and equilibrate much more rapidly than the slow variables (n, c). We call Eq. (4) the *slow system*. An equivalent description of the dynamics can be obtained by

rescaling time $\left(t_s = \varepsilon_2 t_f\right)$ to give the *fast system*:

$$\begin{aligned}\frac{dV}{dt_f} &= \frac{\varepsilon_2}{\varepsilon_1} f_1(V,b,n,c),\\ \frac{db}{dt_f} &= f_2(V,b),\\ \frac{dn}{dt_f} &= \varepsilon_2 g_1(V,n),\\ \frac{dc}{dt_f} &= \varepsilon_2 g_2(V,c).\end{aligned} \tag{4}$$

Systems (4) and (5) are equivalent in the sense that they trace out the same paths in phase space, but at different speeds.

The next step is to take the singular limit to decompose Eq. (1) into slow and fast subsystems that are simpler to analyze. However, the presence of two perturbation parameters naturally leads to the question of which limit to take. Taking the limit $\varepsilon_1 \to 0$ with $\varepsilon_2 \neq 0$ assumes that the voltage variable is significantly faster than the other variables. Similarly, the limit $\varepsilon_2 \to 0$ with $\varepsilon_1 \neq 0$ assumes that the activation of the BK channels is a much more rapid process than anything else. Here, we make the *a priori* assumption that V and b vary on similar timescales. As such, we take the double singular limit $(\varepsilon_1, \varepsilon_2) \to (0,0)$ under the stipulation that the relative speeds of V and b remain comparable. Formally, we assume that

$$\lim_{(\varepsilon_1,\varepsilon_2)\to(0,0)} \frac{\varepsilon_2}{\varepsilon_1} = r, \tag{5}$$

where $r = \mathcal{O}(1)$ so that $\varepsilon_2 = r\varepsilon_1$. Given the relation between ε_1 and ε_2, we now only to refer to ε_2 with the value of ε_1 implied. The (double) singular limit $\varepsilon_2 \to 0$ (and hence $\varepsilon_1 \to 0$) in the fast system (Eq. (5)) leads to the 2D *layer problem*:

$$\begin{aligned}\frac{dV}{dt_f} &= r f_1(V,b,n,c),\\ \frac{db}{dt_f} &= f_2(V,b),\\ \frac{dn}{dt_f} &= 0,\\ \frac{dc}{dt_f} &= 0.\end{aligned} \tag{6}$$

The singular limit $\varepsilon_2 \to 0$ on the slow timescale (i.e. in the slow system (Eq. (4))) gives the 2D *reduced problem*:

$$\begin{aligned}0 &= f_1(V,b,n,c),\\ 0 &= f_2(V,b),\\ \frac{dn}{dt_s} &= g_1(V,n),\\ \frac{dc}{dt_s} &= g_2(V,c).\end{aligned} \tag{7}$$

In terms of matched asymptotic expansions (Mishchenko et al. 1994), the reduced and layer problems correspond to the outer and inner solutions, respectively. The idea of GSPT is to combine the information from the 2D layer problem and the 2D reduced problem in order to gain insight into the original 4D cell model (Eq. (1)). For the scope and purposes of this paper, we avoid excessive mathematical detail and provide only a cursory analysis of the slow and fast subsystems whilst highlighting the features relevant to our problem.

3.1 The layer problem

We begin with a bifurcation analysis of the 2D layer problem (Eq. (6)). The layer problem is an approximation of Eq. (1) in which the slow variables are assumed to move so slowly that they are essentially fixed. That is, the slow variables act as parameters in the layer problem approximation. The set of equilibria for the layer problem is a surface called the *critical manifold*:

$$S := \left\{(V,b,n,c) \in \mathbb{R}^4 : f_1(V,b,n,c) = f_2(V,b) = 0\right\}. \tag{8}$$

Since n and b enter linearly into f_1 and f_2, respectively, we can obtain a graph representation of the critical manifold:

$$\begin{aligned}b &= b_\infty(V),\\ n &= -\frac{1}{g_K}\left(g_{Ca} m_\infty(V)\frac{V-V_{Ca}}{V-V_K} + g_{BK} b_\infty(V)\right.\\ &\qquad \left. + g_{SK} s_\infty(c) + g_L \frac{V-V_L}{V-V_K}\right).\end{aligned} \tag{9}$$

Figure 5a shows an archetypical critical manifold S, drawn as a graph over the slow variables (n,c). We observe that the critical manifold is folded, which is typical of neuronal problems (Teka et al. 2011; Vo et al. 2010; Rotstein et al. 2008; Rubin and Wechselberger 2008; Wechselberger and Weckesser 2009; Ermentrout and Wechselberger 2009). The fold curves, L, of S are precisely the set of points where the layer problem undergoes a saddle-node bifurcation:

$$L := \{(V,b,n,c) \in S : \det \boldsymbol{J}_r = f_{1V} f_{2b} - f_{1b} f_{2V} = 0\}, \tag{10}$$

where $\boldsymbol{J}_r = \begin{pmatrix} r f_{1V} & r f_{1b} \\ f_{2V} & f_{2b}\end{pmatrix}$ is the Jacobian of the layer problem. Note that the condition in Eq. (10) is necessary but not sufficient. In Fig. 5a, there are two fold curves: an upper fold curve L^+ and a lower one L^-. These divide the critical manifold S into attracting sheets, S^a, and repelling sheets, S^r, where the notions of attraction and repulsion come from a linear stability analysis of Eq. (6).

The fold curves are of interest because they are points where Fenichel theory (Fenichel 1979; Jones 1995) breaks down. More generally, Fenichel theory breaks down in the

neighbourhood of bifurcations of Eq. (6). Usually, the interesting dynamics are localized around these non-hyperbolic regions. We note here for later reference that another way in which Fenichel theory can break down is via a Hopf bifurcation of the layer problem (see Section 4.2). The Hopf curves, H, of the critical manifold are given by:

$$H := \{(V, b, n, c) \in S : \text{tr}\, \boldsymbol{J}_r = r f_{1V} + f_{2b} = 0\}, \qquad (11)$$

together with a transversality condition (the eigenvalues of the linearization of Eq. (6) must cross the imaginary axis with non-zero speed)[2]. Again, the condition in Eq. (11) is necessary but not sufficient. For normally hyperbolic critical manifolds (i.e. the eigenvalues of the linearization of Eq. (6) evaluated along S are uniformly bounded away from the imaginary axis), Fenichel theory guarantees the persistence of locally invariant slow manifolds $S_{(\varepsilon_1,\varepsilon_2)}$ of the fully perturbed problem (Eq. (4)) for sufficiently small perturbations.

According to the layer problem, an arbitrary initial condition starting away from the critical manifold will be drawn into one of the attracting sheets of S. Once the trajectory is on the critical manifold, the layer flow predicts trivial dynamics. At this point, the slow processes dominate and the layer flow is no longer a suitable approximation of the dynamics. As such, we must switch viewpoints and consider the slow dynamics via the reduced system.

3.2 The reduced problem

The 2D reduced problem is a differential-algebraic system, consisting of algebraic equations that constrain the dynamics to some surface and differential equations that describe the slow motions along that surface. We observe that the algebraic conditions in Eq. (7) constrain the slow motions to the critical manifold itself. That is, the reduced system (Eq. (7)) prescribes a nontrivial flow along S. Moreover, the restriction of the flow of Eq. (4) to the invariant slow manifolds $S_{(\varepsilon_1,\varepsilon_2)}$ is a small smooth perturbation of the slow flow along S.

To analyze the flow on a manifold, one must typically look at the flow in various coordinate charts (we refer to (Wechselberger 2012) for a more detailed discussion of how to deal with reduced systems in arbitrary dimensions). To obtain evolution equations in all coordinate charts for the reduced problem (Eq. (7)), we take a total time derivative of the algebraic constraints and rearrange to obtain:

$$\begin{pmatrix} -\boldsymbol{J} & \boldsymbol{0} \\ \boldsymbol{0} & \boldsymbol{I}_2 \end{pmatrix} \frac{d}{dt_s} \begin{pmatrix} V \\ b \\ n \\ c \end{pmatrix} = \begin{pmatrix} f_{1n} g_1 + f_{1c} g_2 \\ 0 \\ g_1 \\ g_2 \end{pmatrix}, \qquad (12)$$

where $\boldsymbol{J} = \begin{pmatrix} f_{1V} & f_{1b} \\ f_{2V} & f_{2b} \end{pmatrix}$ is a special case of the Jacobian $\boldsymbol{J}_r$ of Eq. (6), $\boldsymbol{0}$ is the 2×2 zero matrix and $\boldsymbol{I}_2$ is the 2×2 identity matrix. Multiplying both sides by the 4×4 matrix $\begin{pmatrix} -\text{adj}(\boldsymbol{J}) & \boldsymbol{0} \\ \boldsymbol{0} & \boldsymbol{I}_2 \end{pmatrix}$, where $\text{adj}(\boldsymbol{J})$ is the adjoint of $\boldsymbol{J}$, leads to the following form for the reduced system:

$$\begin{pmatrix} (\det \boldsymbol{J})\boldsymbol{I}_2 & \boldsymbol{0} \\ \boldsymbol{0} & \boldsymbol{I}_2 \end{pmatrix} \frac{d}{dt_s} \begin{pmatrix} V \\ b \\ n \\ c \end{pmatrix} = \begin{pmatrix} -f_{2b}\,(f_{1n} g_1 + f_{1c} g_2) \\ f_{2V}\,(f_{1n} g_1 + f_{1c} g_2) \\ g_1 \\ g_2 \end{pmatrix}, \qquad (13)$$

which describes the flow of the reduced problem on S in the 4 coordinates (V, b, n, c). Usually, more than one coordinate chart is needed to cover a manifold. In our case, the critical manifold has a graph representation (9), which allows us to use a single coordinate chart and obtain the projection of the reduced system on the (V, c) plane:

$$\begin{aligned} \det \boldsymbol{J}\, \frac{dV}{dt_s} &= -f_{2b}\,(f_{1n} g_1 + f_{1c} g_2), \\ \frac{dc}{dt_s} &= g_2, \end{aligned} \qquad (14)$$

where b and n are now specified by Eq. (9). The projection of the reduced system (Eq. (14)) highlights an important fact: the reduced system is singular at the fold curves L. However, this singular term can be removed by a time rescaling ($dt_s = (\det \boldsymbol{J})\, dt_d$) to give the *desingularized system*:

$$\begin{aligned} \frac{dV}{dt_d} &= -f_{2b}\,(f_{1n} g_1 + f_{1c} g_2) \equiv F(V, c), \\ \frac{dc}{dt_d} &= (\det \boldsymbol{J})\, g_2. \end{aligned} \qquad (15)$$

Note that in regions where $\det \boldsymbol{J} < 0$, the time rescaling reverses the orientation of trajectories.

The desingularized system possesses two kinds of singularities: *ordinary* and *folded*. Ordinary singularities are simply equilibria of the desingularized system (15), of the reduced system (7) and of the original cell model (1). More precisely, ordinary singularities, E, are given by

$$E := \{(V, b, n, c) \in S : g_1 = g_2 = 0\}. \qquad (16)$$

Folded singularities, M, on the other hand, are points on the fold curve where F vanishes:

$$M := \{(V, b, n, c) \in L : F = 0\}. \qquad (17)$$

In the desingularized system, M is a set of equilibria. However, in the reduced system (Eq. (14)), folded singularities are special points where both sides of the V-equation vanish simultaneously. This means that there is potentially a cancellation of a simple zero, i.e. dV/dt_s is finite and non-zero at a folded singularity. This in turn allows trajectories to cross the fold L in finite time. Such solutions are called *singular canards* and their persistence under small

[2] We point out that for our model equations, $\det J|_S$ and $\text{tr}\, J|_S$ are both independent of the calcium variable c.

perturbations (i.e. ε_2 small and nonzero) gives rise to complex dynamics (see Brøns et al. 2006; Harvey et al. 2011; Rotstein et al. 2008; Teka et al. 2011; Vo et al. 2010; Wechselberger and Weckesser 2009 for examples). There are three generic types of folded singularities (based on the eigenvalues of the linearization of Eq. (15)): folded saddles which have real eigenvalues of opposite sign, folded nodes which have real eigenvalues of the same sign and folded foci which possess complex eigenvalues. Folded nodes have interesting properties and have been shown in various other bursting problems to be a crucial piece of the puzzle (Brøns et al. 2006; Harvey et al. 2011; Rubin and Wechselberger 2008; Teka et al. 2011; Vo et al. 2010).

3.3 Singular orbit construction

The aim of GSPT is to combine information from the reduced and layer problems in order to understand the dynamics of the cell model (Eq. (1)), particularly the oscillatory behaviour. To this end, we now use our reduced and layer flows to construct singular periodic orbits, which according to GSPT (Szmolyan and Wechselberger 2004), will perturb to nearby periodic orbits of the full system (Eq. (1)) for sufficiently small perturbations. We start with the construction of the simplest type of periodic solution of interest: a relaxation oscillation. An example of such a construction is illustrated in Fig. 5. Relaxation oscillations have been carefully studied in a variety of contexts using asymptotic methods (Dorodnitsyn 1947; Grasman 1987; Mishchenko and Rozov 1980). Here, we adopt the geometric approach (Szmolyan and Wechselberger 2004). We first identify the main objects from our singular analysis. The critical manifold S is folded with attracting and repelling sheets (S^a and S^r) separated by the fold curves $L^{\pm}$. There is a folded singularity on each fold curve: a folded node on L^+ and a folded focus on L^-. The full system equilibrium (ordinary singularity, E) lies on the repelling manifold for the chosen parameter set. Note that spiking, bursting and plateauing are only possible provided that E is unstable (i.e. that $E \in S^r$).

Figure 5 shows the singular attractor for the given parameter set constructed from the reduced (outer solution) and layer (inner solution) flows. The singular orbit consists of 4 distinct segments. Starting at the lower fold curve L^-, there is a rapid evolution described by Eq. (6) towards the upper attracting manifold S^a (red, double arrow). Once the trajectory reaches S^a, the reduced flow description (Eq. (7)) takes over until the trajectory (denoted by Γ_S) reaches the upper fold L^+. At the fold curve, the reduced flow is singular and there is a finite time blow-up of the solution (i.e. the solution ceases to exist). As such, the layer problem becomes the appropriate descriptor and there is a fast down-jump to the lower attracting manifold. From there, the reduced system describes the slow motions along the critical manifold until the trajectory once again hits the fold curve, thus completing the orbit. GSPT then guarantees that this singular orbit will persist as a nearby periodic relaxation oscillation corresponding to a spiking solution of Eq. (1).

4 Canard- and Hopf-induced MMOs

Having seen how to use the reduced and layer problems to construct singular periodic orbits, we are now in a position to investigate the oscillatory behaviour of Eq. 1. There are two distinct mechanisms by which MMOs can be generated: canard dynamics and slow passage through a dynamic Hopf bifurcation (we refer to Section 9 of

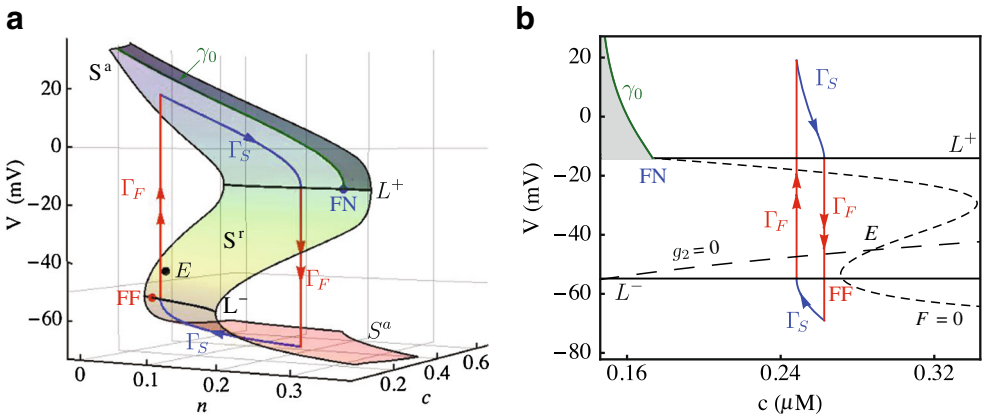

Fig. 5 Critical manifold and singular periodic orbit constructed from Eqs. (6) and (7), projected onto **a** (V, n, c) space and **b** the (V, c) plane for $g_K = 3.2$ nS, $g_{BK} = 0.05$ nS, $r = 1$ and all other parameters set to their standard values. The critical manifold S is folded with fold curves $L^{\pm}$. On L^+ (L^-), there is a folded node (folded focus). The singular orbit consists of slow orbit segments Γ_S along the attracting branches S^a together with fast jumps Γ_F between them. The fast up-jump projects the singular orbit outside the funnel of the folded node, which is bounded by L^+ and the strong canard, γ_0 (see Section 4)

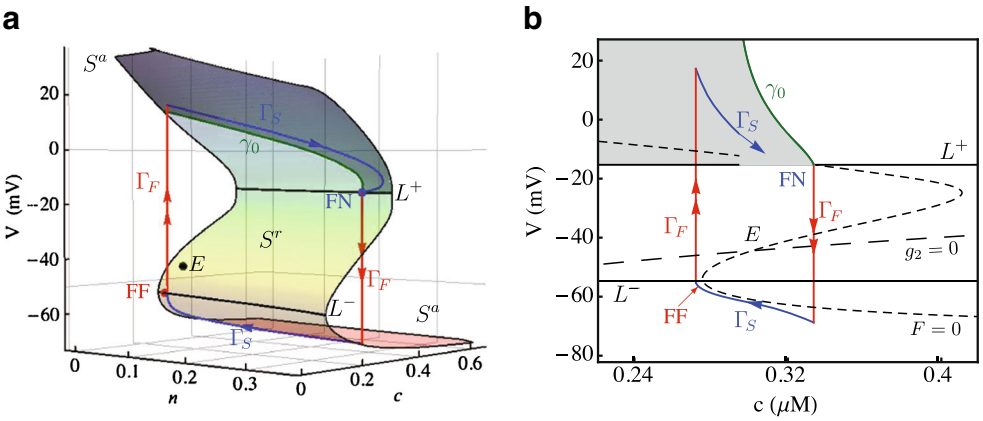

Fig. 6 Singular orbit construction in the case of a canard-induced MMO for $g_{BK} = 0.1$ nS and $r = 1$ with all other parameters as in Table 1. There is a folded node on L^+ and the fast up-jump of the singular orbit returns it to the funnel (shaded region between the fold L^+ and the strong canard γ_0) of the folded node

Desroches et al. (2012) for a comprehensive account of MMOs in the literature). Canard dynamics are associated with the slow subsystem and have been found in other neuroendocrine cell models to be the progenitor for the bursting behaviour (Teka et al. 2011; Vo et al. 2010, 2012). The slow passage through a dynamic Hopf bifurcation can be observed when there is a Hopf bifurcation in the fast subsystem that is unrelated to equilibria of the full system (Bertram et al. 1995; Rinzel 1985; Stern et al. 2008; Teka et al. 2011; Osinga and Tsaneva-Atanasova 2010; Tsaneva-Atanasova et al. 2010). In this section, we examine both mechanisms in detail and demonstrate the origin of the bursting behaviour.

4.1 Canard dynamics

As we saw in Section 3.2, the folded singularities can lead to counter-intuitive behaviour due to the indeterminate form for the V-equation in Eq. (14). More specifically, it is possible for trajectories that reach the folded singularity to pass through it with finite speed. This potential for trajectories to tunnel through the fold is the linchpin of the argument for the burst generating mechanism in *canard-induced MMOs*. Here, we illustrate how this tunnelling behaviour can lead to the small oscillations of a burst.

Figure 6 shows a singular orbit construction in which there is a folded node on the upper fold curve L^+. Associated to the folded node is a subset of the attracting manifold S^a called the *funnel* of the folded node (grey shaded region). The funnel is bounded by the fold curve L^+ and by the *strong canard* γ_0, which is the unique trajectory tangent to the strong eigendirection of the folded node. Every trajectory that lands inside the funnel region is inevitably drawn into the folded node. We quantify this by introducing a metric δ, which measures the distance from the landing point of the singular orbit on its fast up-jump to the strong canard γ_0. By convention, we say that trajectories that land inside the funnel have a positive δ and trajectories that land outside the funnel have a negative δ. Singular canards are identified as those trajectories with a positive δ. These special solutions start on S^a, tunnel through the fold L^+ (via the folded node) and follow S^r for $\mathcal{O}(1)$ times on the slow timescale before they are repelled[3].

There are two requirements for the existence of canard-induced MMOs (Brøns et al. 2006): the reduced flow must possess a folded node and there must be some kind of global re-injection mechanism (fast depolarization) that returns trajectories to the funnel of the folded node. This second condition is equivalent to the requirement that δ is positive or, in other words, that there is a singular periodic orbit that initiates its down jump at the folded node. According to canard theory, such a singular periodic orbit will perturb to a MMO orbit for sufficiently small perturbations $\mathcal{O}(\varepsilon_2)$. Moreover, the small amplitude oscillations of the MMO occur in a neighbourhood of the folded node (Fig. 7). Furthermore, the maximal amplitude of these small oscillations is $\mathcal{O}\left(\sqrt{\varepsilon_2}\right)$. The rotational behaviour in a neighbourhood of the folded node arises from geometric properties of invariant slow manifolds. We refer to Brøns et al. (2006), Wechselberger (2005) for details.

Figure 7 shows how the singular canard orbits perturb to MMOs for fixed ratio r and various perturbations ε_2. Note that the full system trajectory (black orbit) initially approaches the folded node parallel to the strong eigendirection. This brings the trajectory close to the folded node, where the trajectory then follows the weak eigendirection (which serves as a linear approximation to the axis of rotation for the small oscillations). Subsequently, the full system orbit spends a significant amount of time on the repelling manifold before jumping away. The deeper into the funnel the singular orbit lands, the more time that the full

[3]Folded nodes have a sector of canards (the funnel). Folded saddles have precisely two canards (tangent to the eigendirections of the folded saddle) and folded foci have no canards.

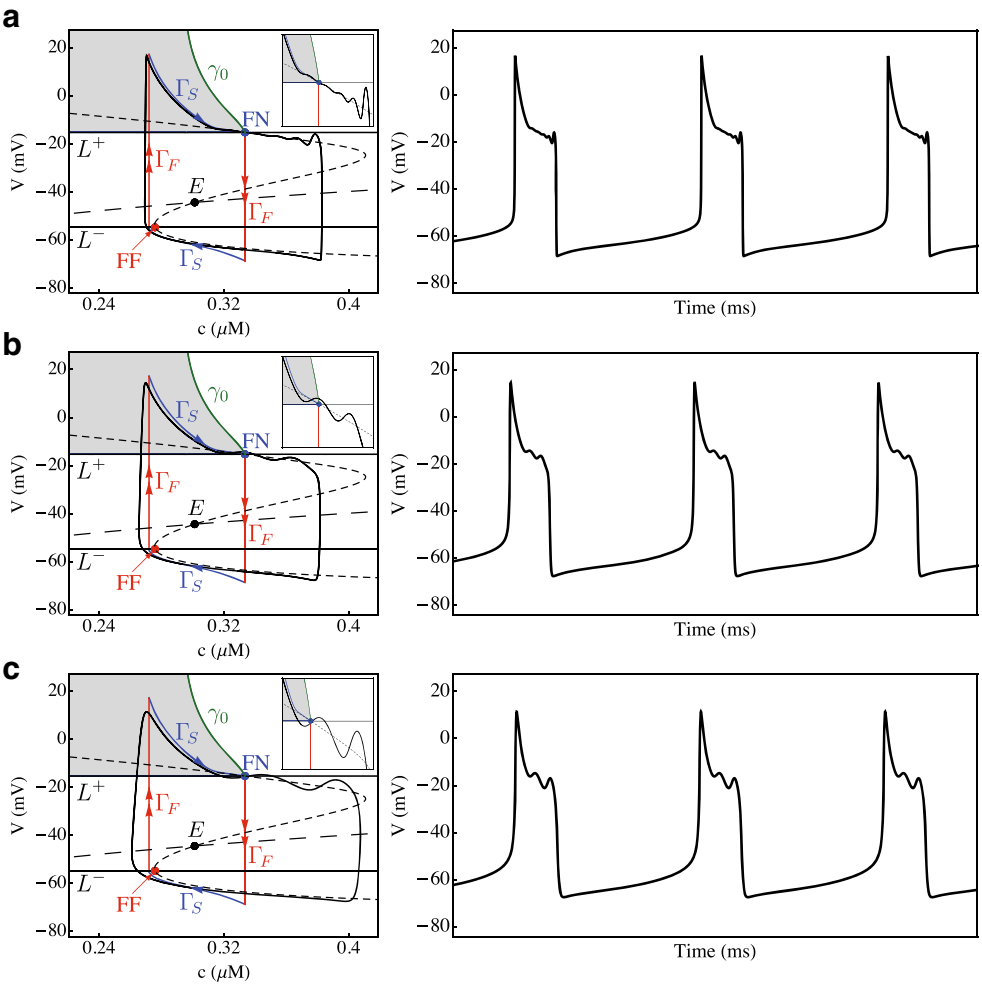

Fig. 7 Canard-induced MMOs for $g_{BK} = 0.1$ nS, $r = 1$ and **a** $C_m = 0.5$ pF, $\tau_{BK} = 0.5$ ms, **b** $C_m = 2$ pF, $\tau_{BK} = 2$ ms and **c** $C_m = 5$ pF, $\tau_{BK} = 5$ ms (cf. Fig. 6). The left panels show the singular ($\Gamma_F \cup \Gamma_S$) and non-singular orbits in the (V, c) plane. The right panels show the associated time courses. The parameters C_m and τ_{BK} were chosen to preserve the ratio $r = 1$. The small oscillations are localized about the folded node and their amplitudes increase with the perturbation parameters (C_m, τ_{BK}). The parameter set in panel (c) places the trajectory on the lower dashed line in Fig. 4a

system trajectory spends on the repelling sheet and the more small oscillations executed in the full system trajectory. We note here that there is an upper bound, $s_{\max}$, on the number of small oscillations that a canard-induced MMO may have (see Brøns et al. 2006; Wechselberger 2005). Only MMOs with $s < s_{\max}$ have easily observable small amplitude oscillations whilst the small oscillations in MMOs with $s = s_{\max}$ are usually very difficult to observe (see Section 3.1 of Desroches et al. (2012) for example).

Variations in the system parameters alter the landing point of the fast up-jump of the singular orbit. If the parameters are calibrated so that the fast up-jump projects the singular orbit into the funnel far from the strong canard γ_0, then the full system trajectory will execute $s_{\max}$ oscillations (for sufficiently small perturbations). Whether or not these sub-threshold oscillations are actually observable is a different matter. As the landing point of the fast up-jump moves (under parameter changes) and approaches γ_0, fewer small oscillations will be observed in the burst pattern and the time spent on the repelling side of the manifold decreases. When $\delta < 0$ (Fig. 5), the singular orbit never passes through the folded node and hits L^+ at a regular jump point. Consequently, singular orbits with $\delta < 0$ perturb to regular spiking behaviour.

4.2 Slow passage through a dynamic Hopf bifurcation

Canard-induced MMOs arise from the canard dynamics associated with folded node singularities in the slow subsystem (Eq. (7)) and provide one burst generating mechanism. However, as suggested by Figs. 2 and 3, changes in the system parameters can drastically alter the MMO trajectories and the mechanisms that generate them. More precisely, changes in g_{BK} change the shape and structure of the critical manifold. For this reason, we now consider MMOs generated from a slow passage through a dynamic Hopf bifurcation (Baer et al. 1989; Neishtadt 1987, 1988) of the fast subsystem (Eq. (6)). Figure 8 shows the singular orbit construction in the case of Hopf-induced MMOs. The major difference from the canard case is that there is now a curve of Hopf bifurcations H on S. To be precise, these are subcritical Hopf bifurcations of the layer problem (Eq. (6)) so

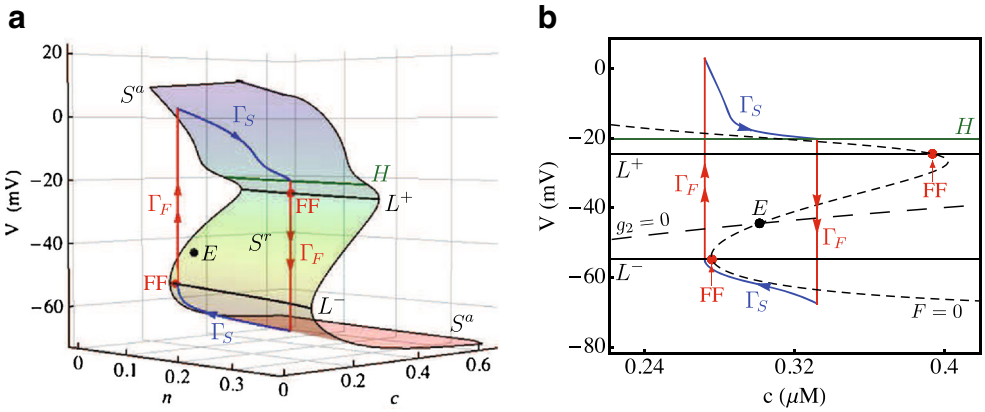

Fig. 8 Singular orbit construction in the case of Hopf-induced MMOs for $g_{BK} = 0.5$ nS and $r = 1.2$. The repelling manifold is enclosed by the Hopf curve H and the lower fold curve L^-. Note that the folded singularity on L^+ is now a focus instead of a node and the change in the structure of S is due to the increase in g_{BK} (see Fig. 11)

that the associated bursts are pseudo-plateau type[4]. For a fixed c, the periodic branch that emanates from H is unstable (along the entire branch) and terminates at a homoclinic on the repelling sheet of S. To simplify the presentation, we omit these (unstable) periodic branches from Fig. 8 and focus only on the key organizing structures.

In Fig. 8, it is clear that the Hopf curve occurs at a more depolarized voltage level than the upper fold L^+. This means the repelling sheet of S extends past the upper fold L^+ and is now enclosed by H and L^-. Since the upper attracting sheet of the critical manifold terminates at the curve of Hopf bifurcations H, the corresponding singular orbit must jump at H, where the stability changes. In the full system trajectory however, there is a substantial delay before the trajectory jumps to the lower attracting manifold, with small amplitude oscillations visible just before the jump (Fig. 9a). This delay is mainly observed for small perturbations $\mathcal{O}(\varepsilon_2)$. For larger perturbations, the delay is less substantial and the small oscillations are observed on both sides of the Hopf bifurcation (Fig. 9b and c).

The flow of Eq. (1) in a neighbourhood of H can be understood in very simple terms. For $\varepsilon_2 = 0$, the slow variables (n, c) are fixed parameters of the layer problem (Eq. (6)). For $\varepsilon_2 \neq 0$, n and c are dynamic quantities that drift through the vicinity of the Hopf curve. As the trajectory approaches H from the attracting side, the eigenvalues of Eq. (6) are complex with negative real part. Exponential contraction of the system means that the trajectories become exponentially close to S^a on the slow timescale. As the trajectory passes H over to the repelling sheet of S, the real part of the eigenvalues crosses zero and becomes positive. However, the trajectories are not immediately repulsed. Instead, the trajectories destabilize when the expansion on the repelling manifold counteracts the accumulative contraction on the attracting manifold, which is the cause for the observed delay. The implication then is that the further the trajectory is from H on the attracting side, the longer the delay on the repelling side before it is repelled. However, there is a maximal distance (independent of ε_2) that trajectories may trace the repelling manifold before they must jump away. For further details, we refer to Baer et al. (1989), Neishtadt (1987, 1988).

Much like canard-induced MMOs, the amplitude and number of small oscillations associated with Hopf-induced MMOs is related to the size of the perturbation (i.e. to the amount of time spent in a neighbourhood of H). For small perturbations, the passage through H is slow and the trajectories are exponentially attracted to S^a. As such, there is a substantial amount of time for the trajectories to oscillate but those oscillations are very small and difficult to observe due to the strong attraction to S^a. Any oscillatory behaviour only becomes visible just before the trajectory jumps away when the repulsion along S^r overwhelms the accumulative contraction on S^a. When the perturbation parameter ε_2 is increased, the timescale separation weakens, essentially making the slow variables faster. Consequently, the drift through H is faster and there is less time for the trajectories to oscillate. However, since the attraction to S^a is weaker (due to larger ε_2) the small oscillations have larger amplitude and are easier to observe. Thus, as the perturbation is pushed further, the trajectories have even less time to be pulled into S^a and so the observed oscillations are larger and fewer, since the amount of time spent near H decreases (compare the panels of Fig. 9). Moreover, since the trajectory is drifting through a Hopf bifurcation, the real part of the eigenvalues increases through zero. As such, the small oscillations of the Hopf-induced MMOs initially have decreasing amplitude (on the attracting side) and then increasing amplitude (on the repelling side).

[4]In the classic slow-fast approach to bursting, the criticality of the fast subsystem Hopf differentiates between plateau and pseudo-plateau bursting. Plateau (pseudo-plateau) bursts are associated with supercritical (subcritical) Hopf bifurcations of the layer problem. For further details, we refer to Stern et al. (2008), Osinga and Tsaneva-Atanasova (2010), Tsaneva-Atanasova et al. (2010), Teka et al. (2011).

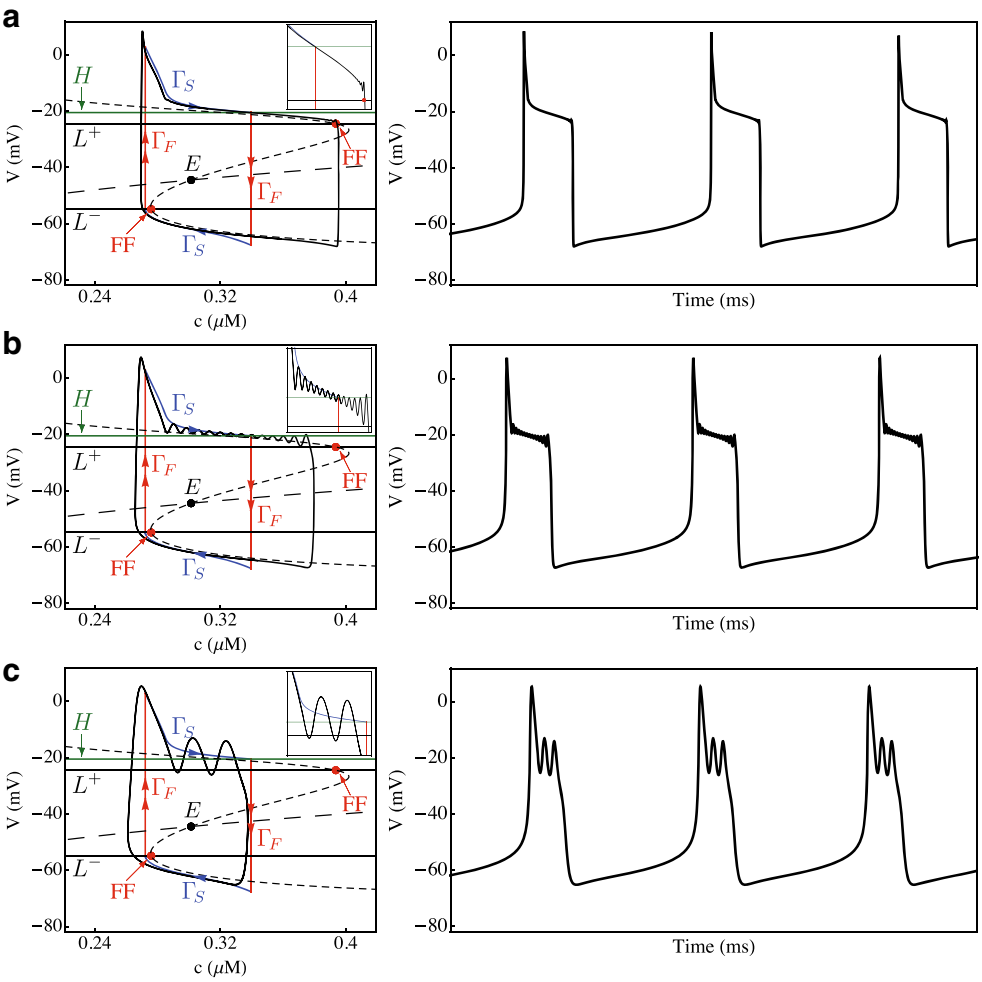

Fig. 9 Hopf-induced MMOs for $g_{BK} = 0.5$ nS, $r = 1.2$ and **a** $C_m = 0.5$ pF, $\tau_{BK} = 0.6$ ms, **b** $C_m = 2$ pF, $\tau_{BK} = 2.4$ ms and **c** $C_m = 5$ pF, $\tau_{BK} = 6$ ms (cf. Fig. 8). The parameter set in panel (c) places the trajectory in the bursting/plateauing region of Fig. 4a. Note that the choices of C_m and τ_{BK} adhere to the ratio $r = 1.2$. Smaller perturbations increase the amount of time spent on S^r but the oscillations have smaller amplitude. Larger perturbations increase the amplitude of the spikes but reduce the amount of time spent near the Hopf curve H

4.3 Damped oscillations jumping at a fold

An important factor in shaping the trajectories is the amount and type of contraction along the slow flow on S^a. When the eigenvalues of Eq. (6) evaluated along slow orbit segments on S^a are real, the trajectories are attracted (or repelled) along nodes of Eq. (6). When the eigenvalues are complex, the attraction (or repulsion) occurs along foci of the layer problem, resulting in oscillatory behaviour in the full system trajectory. With the results of Sections 4.1 and 4.2 in mind, we are now in a position to investigate the geometry and nature of the orbits under parameter changes. A key parameter that influences the amount and type of contraction along S^a is the ratio of fast timescales r. In Fig. 10, we examine the effect of variations of r on the MMOs[5].

Each panel of Fig. 10 shows 2 plots. In the main plot, the singular orbit construction (red and blue) together with the full system trajectory (black) are shown in the (V, c) plane. In the adjacent plot, the real part of the eigenvalues λ of Eq. (6) evaluated along the slow orbit segment Γ_S on S^a is shown (with V on the vertical axis with the same scale as in the main plot). The eigenvalues become complex when the blue curves coalesce and become a single branch. In panel (a), the eigenvalues of Eq. (6) on the stable top sheet are initially real and negative. That is, the trajectory approaches the attracting manifold along nodes of the layer problem. As the reduced flow brings the trajectory towards the Hopf curve, λ becomes complex. However, this region of complex eigenvalues is short lived and the Hopf bifurcation is encountered shortly after. As a result, the full system trajectory has insufficient time to oscillate (for the chosen perturbation parameters) and the associated pattern is a spike. In panel (b), the region of complex λ is more extensive, which provides the full system trajectory just enough time to perform one small oscillation before jumping away. As the ratio r of the speeds of V and b is decreased (i.e. the BK activation made faster), the region of complex eigenvalues becomes more extensive (panels (c) and (d)). The full system trajectories are then able to spend more time in the oscillatory regime resulting in more sub-threshold

[5]Variations in r have no effect on the singular canards since they are associated with the slow subsystem and r is only present in the fast subsystem.

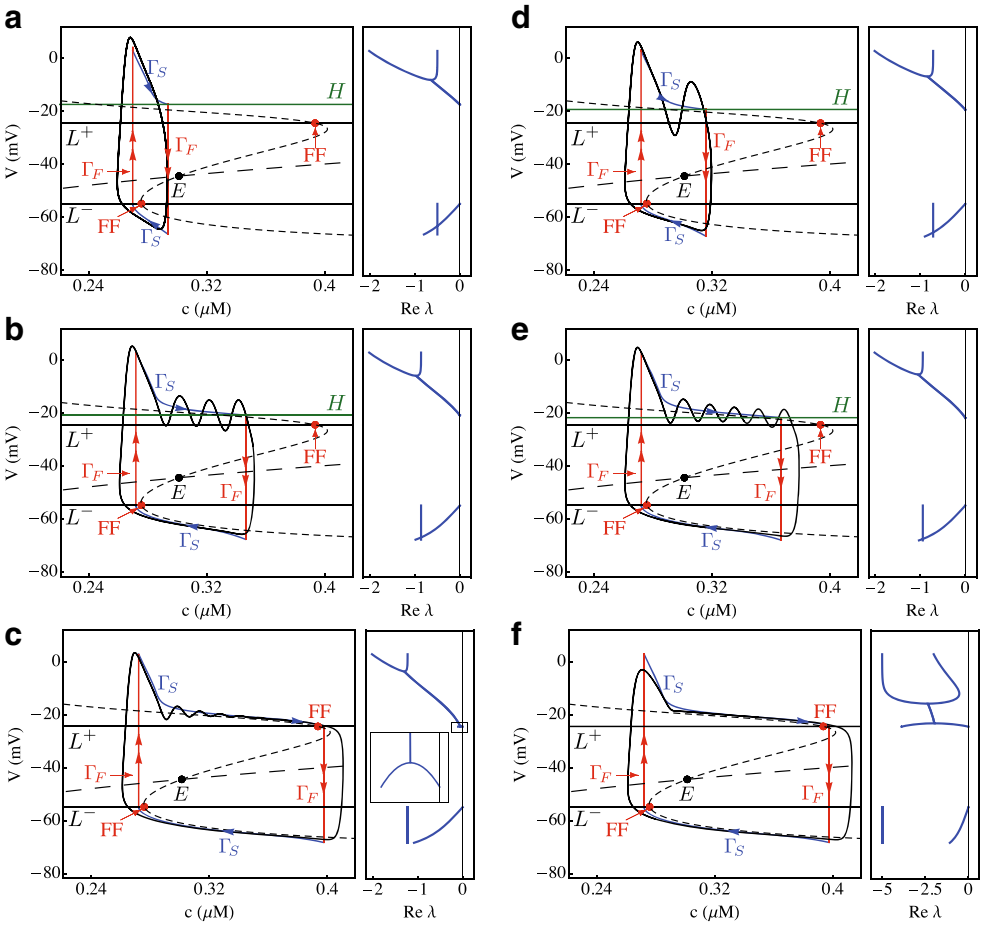

Fig. 10 The eigenvalues of Eq. (6) evaluated along Γ_S regulates the type of bursting pattern. Singular and non-singular orbits are shown for $C_m = 5$ pF, $g_{BK} = 0.5$ nS and **a** $\tau_{BK} = 10$ ms ($r = 2$), **b** $\tau_{BK} = 7$ ms ($r = 1.4$), **c** $\tau_{BK} = 5.8$ ms ($r = 1.16$), **d** $\tau_{BK} = 5.3$ ms ($r = 1.06$), **e** $\tau_{BK} = 4$ ms ($r = 0.8$) and **f** $\tau_{BK} = 1$ ms ($r = 0.2$). The inset in (e) shows the second degenerate node and switch from complex to real eigenvalues. Note the shifted scale on Re λ in (f). The parameters were chosen to correspond to those in Fig. 2

oscillations. Of course, decreasing both perturbation parameters τ_{BK} and C_m (instead of τ_{BK} alone) improves the singular limit predictions and generates more oscillations of smaller amplitude (cf Fig. 9). Note that changing τ_{BK} and C_m (with r fixed) leaves the location of the Hopf curve unaltered, but changes the speed at which the full system trajectory passes through it.

As r decreases further, the Hopf curve H moves closer and closer to the fold curve L^+. Eventually, at some critical r-value, the Hopf and (upper) fold curves coalesce resulting in a double zero eigenvalue, i.e. a Bogdanov-Takens (BT) bifurcation, of the layer problem. This change in the eigenvalue structure of Eq. (6) significantly alters the behaviour of the singular orbits and their non-singular counterparts. Before the BT bifurcation when the repelling manifold S^r is enclosed by H and L^-, the eigenvalues of Eq. (6) along Γ_S are initially real (at the landing point after the fast up-jump). The slow flow then moves the singular orbit through a degenerate node of Eq. (6) and λ becomes complex and remains so until the singular orbit reaches the Hopf curve. In the full system trajectory, this is seen as oscillatory behaviour with decreasing amplitude, since the real part of the eigenvalues increases towards zero.

After the BT bifurcation, the Hopf curve disappears and the repelling sheet of S is enclosed by L^+ and L^-. As before, the eigenvalues of the layer problem along Γ_S are initially real and the slow flow moves the orbit through a degenerate node of Eq. (6) where the eigenvalues become complex. The difference this time is that Γ_S passes through another degenerate node and λ becomes real once again (panels (e) and (f)). This second degenerate node is born at the BT bifurcation and moves away from L^+ to more depolarized voltage levels as r is decreased. The slow flow Γ_S on the upper attracting sheet S^a can then be decomposed into 3 distinct segments. The 'upper' part of Γ_S is the segment between the landing point of the fast up-jump and the first degenerate node of Eq. (6). The 'middle' part is the segment enclosed by the two degenerate nodes and the 'lower' part is the segment between the second degenerate node and L^+. The 'upper' part of Γ_S manifests in the fully perturbed problem as a monotone decrease to more hyperpolarized voltage levels. The 'middle' part corresponds to decaying oscillations in the full system trajectory. The 'lower' segment corresponds to a plateau phase of the full system orbit, where there is only contraction (via nodes of the layer problem) and the small oscillations die out. Smaller ratios r

move the second degenerate node to more depolarized V levels, which causes greater damping of the small oscillations in the active phase (compare panels (e) and (f)). Thus, variations in the ratio r can convert the full system trajectory from spiking to bursting to plateauing. In particular, the jumping mechanism for the singular orbits changes at the BT bifurcation of Eq. (6).

5 Distinguishing between Canard- and Hopf-induced MMOs

In Section 2.2, we showed 2-parameter diagrams illustrating that there are parameter regimes where BK current activated at just the right speed is crucial for bursting. We also demonstrated that there are parameter regimes where the bursting can exist independent of the BK current or its activation speed. We then proceeded to show in Section 4 how the MMOs can arise from two substantially different mechanisms. In this section, we explain the difference between the different regimes encountered in Fig. 4 and discuss the possibility of canard- and Hopf-induced MMOs in real cells.

5.1 MMOs in theory

So far, we have examined in Section 2.2 the effect of variations of g_{BK} and τ_{BK} on the MMOs. We have also demonstrated in Section 4.3 that the ratio r of fast timescales plays a crucial role in determining the nature of the orbit. However, BK current is not the only instigator for bursting and other ionic currents contribute to shaping the electrical activity. Here, we illustrate in (g_K, g_{BK}, r)-space how the oscillation mechanism can change under parameter variations. Figure 11a shows a 2-parameter bifurcation diagram of the reduced system (Eq. (7)) in (g_K, g_{BK}) for an unspecified r (recall that r is not in the slow subsystem). The red boundary (denoted DFN) corresponds to degenerate folded nodes of Eq. (7), where the folded singularity switches from node to focus. In the region of folded nodes (to the right of the DFN curve), canard-induced MMOs can only exist provided $\delta > 0$ i.e. provided the singular orbits are returned to the funnel of the folded node. The blue curve denotes the parameter set where $\delta = 0$. For the region denoted by $\delta < 0$, the folded node and the singular funnel exist, but the singular orbits are projected outside of the funnel region. In the deterministic setting, this guarantees spiking behaviour. However, stochastic fluctuations in actual single-cell recordings may occasionally re-inject trajectories into the funnel of the folded node, thus producing an occasional burst. To the authors' knowledge, studies of how stochastic noise affects canard dynamics are currently scarce (Berglund et al. 2012; Kuehn 2011). A precise characterization of how stochastic fluctuations influence the

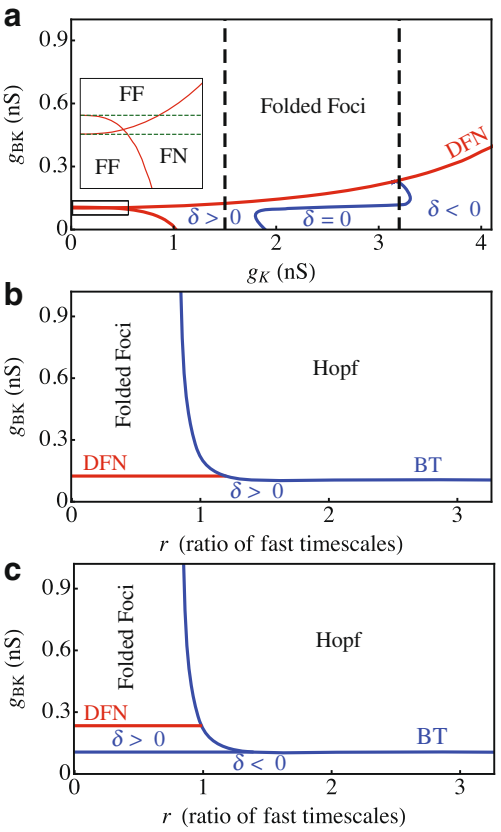

Fig. 11 2-parameter bifurcation diagrams showing changes in the oscillation mechanism in **a** (g_K, g_{BK})-space for unspecified r, **b** (r, g_{BK})-space for $g_K = 1.5$ nS and **c** (r, g_{BK})-space for $g_K = 3.2$ nS. Below the BT line, the Hopf curve does not exist and the folded singularity is either node or focus. The vertical dashed lines in (a) indicate the g_K slices taken in panels (b) and (c)

dynamics is beyond the scope of the current article and is left to future work. Above the DFN border, the folded singularity on L^+ is of focus type and oscillatory behaviour due to canard dynamics is impossible.

The inset of Fig. 11a shows a zoom of the DFN boundary where the 2 red curves cross. This seemingly unusual behaviour can be explained via the geometry of the critical manifold. Firstly, we note that the fold condition (Eq. (10)) is independent of g_K (and g_{SK}). Changes in g_{BK} can alter the location and number of solutions to Eq. (10). For small g_{BK}, there are 2 fold curves $L^{\pm}$. For $g_{BK} \in [0.1025, 0.1067]$ nS (the boundaries of which are shown as green dotted lines in the inset only), the shape of the critical manifold changes and there are 4 folds, $L^{\pm}$, L^{++} and L^{+-}, where the new folds lie between $L^{\pm}$ and L^{++} is above L^{+-}. For $g_{BK} > 0.1067$ nS, L^{++} merges with L^+ and annihilates it in the process, leaving only L^{+-} and L^-. That is, the upper red curve is the DFN boundary for the folded singularity on L^{+-} and the lower red curve is the DFN boundary for the folded singularity on L^+. For the unlabelled region between the two DFN curves where there are 4 folds, the

uppermost fold curve is L^+ and the folded singularity is still a focus. For g_{BK} between the green boundaries where there are 4 folds, the singular orbit construction changes in a very minor way and the analysis from Section 4 holds.

Now, recall from Section 4.3 that the layer problem (Eq. (6)) may undergo a BT bifurcation under parameter variations[6]. In Fig. 11b and c, we show the curve of BT bifurcations (blue curve) in (r, g_{BK})-space[7]. To the right of the BT curve, the singular orbits encounter the Hopf curve before the fold curve and so the corresponding trajectories of Eq. (1) exhibit Hopf-induced MMOs. Whether or not the full system trajectory actually exhibits small oscillations in these regions of parameter space depends entirely on the magnitude of the perturbations. To the left of the BT border, the Hopf curve disappears and the singular orbits jump at the fold curve. In cases where the singular orbit jumps from a folded node ($\delta > 0$), this leads to canard-induced MMOs. Regions where the singular orbits land outside the funnel ($\delta < 0$) correspond to spiking trajectories. Meanwhile, regions labelled folded foci possess a folded singularity of focus type on L^+ (but the singular orbit may jump from a regular jump point). In any case, the full system trajectory in these folded foci regions is a plateau oscillation.

Using our singular analysis, we can now explain the difference between Fig. 4a and b. In Fig. 4a, bursting can exist without any BK current. The speed of BK channel activation only becomes important when g_{BK} exceeds a certain value. In Fig. 11b, this switch in the importance of τ_{BK} is revealed to be due to a switch in the burst generating mechanism. For small g_{BK}, the singular orbits jump from a folded node and the MMOs are of canard type. As such, variations in τ_{BK} (a quantity associated with the fast subsystem) have little impact on the trajectories (see Fig. 3). Beyond the g_{BK} threshold, the burst generating mechanism switches from canard dynamics to slow passage through a dynamic Hopf bifurcation and τ_{BK} becomes a crucial factor in determining the shape of the trajectories (see Fig. 2). In Fig. 4b, BK current is essential for bursting. Figure 11c reveals why this is so. For small g_{BK}, folded nodes exist in Eq. (7) but the singular attractor always lands outside the funnel region. The addition of g_{BK} moves the singular orbits into the funnel region and then eventually, for sufficiently large g_{BK}, changes the MMO mechanism. All together, what Fig. 11 illustrates is that the canard- and Hopf-induced MMOs are generic features and both mechanisms must be taken into consideration in order to understand the dynamics of Eq. (1).

[6]In our case, the homoclinic associated with the BT bifurcation has no influence on the full system dynamics.

[7]The BT bifurcation is a codimension 2 bifurcation. The reason we are able to draw a curve of BT bifurcations is that $\det J|_S$ and $\mathrm{tr}\ J|_S$ are both independent of c

5.2 MMOs in practice

We have demonstrated the existence of both canard- and Hopf-induced MMOs in Eq. (1). The question then is whether or not they are observed experimentally. A simple test to distinguish between the canard and Hopf-induced MMOs is to inject artificial BK current (via dynamic clamp) and vary τ_{BK}. Based on our full system bifurcation analysis (Section 2.2) and our geometric singular perturbation analysis (Section 4), we expect (for fixed C_m) the canard-induced MMOs to have weak response to variations in τ_{BK}, whilst the Hopf-induced MMOs should have extreme sensitivity to variations in τ_{BK}. To test the sensitivity of the trajectories to variations in τ_{BK}, we blocked the BK channels using paxilline and measured the response of the cell to injection of BK current at different activation rates. The injected g_{BK} values were chosen close to the minimum needed to evoke bursting (otherwise we would be in the high g_{BK} regime where there are no canard dynamics).

The dynamic clamp technique is an electrophysiological technique whereby a current, computed from mathematical models, is injected into a cell to simulate dynamic processes (Sharp et al. 1993). The current of interest in our case is I_{BK} with its model equation given in Eq. (2). In order to update the BK activation variable b and driving force $V - V_K$, information on the voltage V is required. In the dynamic clamp technique, rather than using a model for V, the voltage is recorded in real time from the cell and used in calculations. Thus, the computer calculates the model I_{BK} using V from the cell, then injects the model current into the cell. This two-way interaction is done rapidly, at average time steps of 54 μs.

In Fig. 12, we show evidence for Hopf-induced MMOs in pituitary cells. Panels (a) to (d) show the effect of varying the activation time constant τ_{BK} for fixed g_{BK}. For BK current injected with slow activation time constant (i.e. τ_{BK} large), the cell is in a spiking state (panel (a)). By decreasing the activation time constant, we eventually cross a threshold and bursting can be observed interspersed with the spiking activity (panel (b)). Further decreasing τ_{BK} reliably converts the electrical activity to bursting and the spiking behaviour is absent (panel (c)). Moreover, the amplitude of the small oscillations decreases with τ_{BK}. For sufficiently fast activation rates, the small oscillations are virtually nonexistent and the electrical activity exhibits plateau behaviour (panel (d)). These observations are consistent with the prediction that for Hopf-induced MMOs, decreasing τ_{BK} switches the activity from spiking to bursting to plateauing (Fig. 10).

To quantify how changing τ_{BK} affects the electrical activity, we first measured the amplitude of the largest sub-threshold oscillation in a given burst for a fixed g_{BK} with activation time constant τ_{BK}. We then normalized

the amplitude relative to the maximum and minimum voltage values of that burst to obtain the maximal relative amplitude. Averaging over the number of events (where an 'event' refers to a spike, burst or plateau) produced the mean maximal sub-threshold oscillation amplitude for a fixed (τ_{BK}, g_{BK}) pair. This procedure was repeated for each (τ_{BK}, g_{BK}) pair used in the dynamic clamp experiments. Figure 12e provides a graphical summary of the amplitude data from these experiments for 5 cells (different curves). Bursting appears for fast activation rates with sub-threshold oscillations of large amplitude (relative to the size of the pulse). For very fast BK activation, the mean maximal sub-threshold oscillation amplitude decreases and eventually disappears, giving way to plateaus. Figure 12f shows an equivalent diagram to panel (e) for system (1) with $C_m = 5$ pF, $g_K = 3.2$ nS and $g_{BK} = 0.5$ nS (with parameters chosen so that the MMOs are Hopf-type). The model predicts the trends observed experimentally. Namely, that fast BK activation generates bursting with small oscillations that decrease in amplitude as τ_{BK} is decreased.

The dynamic clamp data provides direct evidence for the Hopf mechanism. Evidence for the canard-induced MMOs is more elusive. One example where the canard-induced MMOs may explain the behaviour is in the case of blocking of the BK channels. Many cells in an unstimulated state either burst or spike. For those cells that are initially bursting, introducing the BK channel blocker paxilline usually ceases the bursting activity and results in spiking. In mathematical terms, this is due to the loss of a fast variable making the Hopf mechanism impossible. However, there are some cells (about 10 % of those tested) where the bursting activity persists in the presence of paxilline or other BK channel blockers (Tabak et al. 2011). As this leaves only one fast variable remaining in our model, then according to Eq. (1) the bursting must arise from canard dynamics. However, this persistence of bursting after BK block was only observed in a minority of cells. Moreover, models of cell activity that contain more ionic currents will also have more fast variables, making it feasible to have Hopf-induced MMOs in the presence of BK blockers.

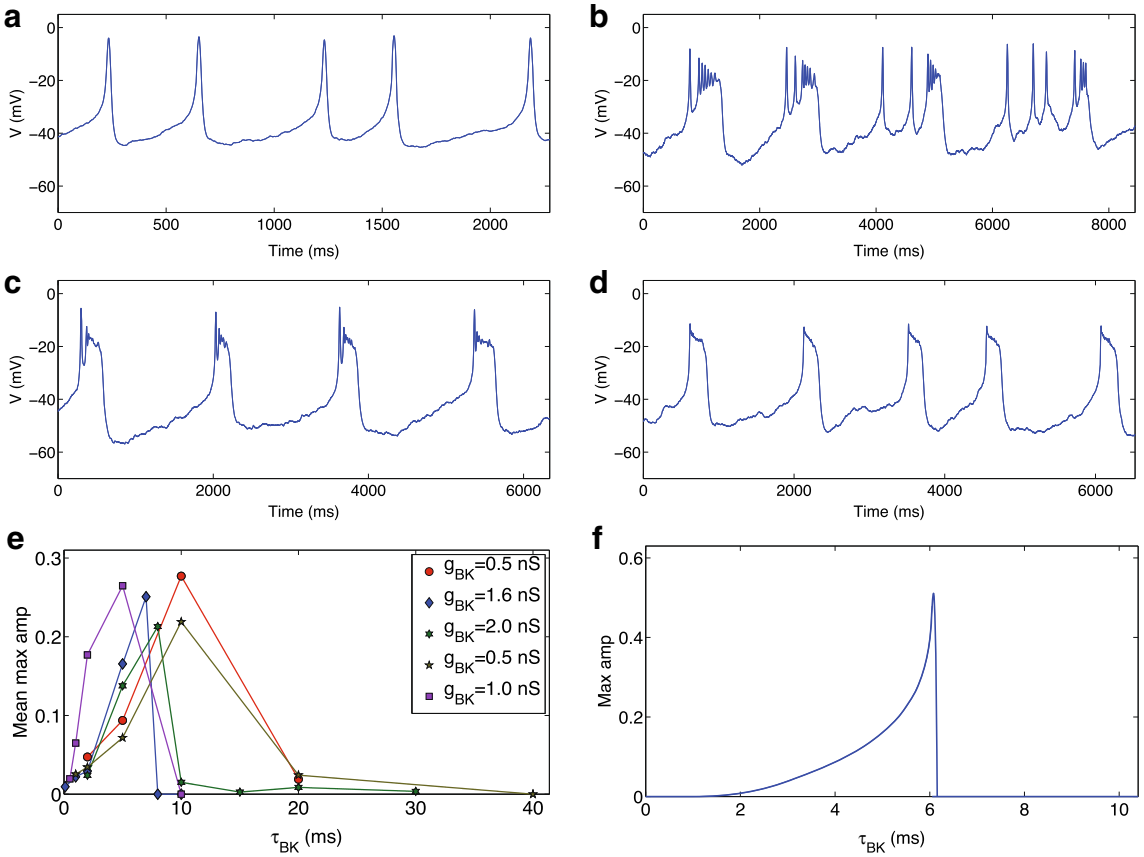

Fig. 12 Effect of variations of τ_{BK} in dynamic clamp experiments. For **a** $\tau_{BK} = 10$ ms, the cell is spiking. In **b**, $\tau_{BK} = 7$ ms, which is at the bursting threshold and the time course is a mixture of spikes and bursts. In **c**, $\tau_{BK} = 5$ ms and the cell is bursting. In **d**, $\tau_{BK} = 2$ ms and the electrical activity consists of plateau patterns. Note the different timescales. A summary of the behaviour of the sub-threshold oscillation amplitude under τ_{BK} variations in five different cells is presented in panel (e). The g_{BK} values for the circle, diamond, hexagram, pentagram and square marker points are $g_{BK} = 0.5, 1.6, 2, 0.5, 1$ nS, respectively. The cell in panels (a) to (d) corresponds to the diamond marker points ($g_{BK} = 1.6$ nS). Panel **f** shows the same figure for the model (1) with $C_m = 5$ pF, $g_K = 3.2$ nS and $g_{BK} = 0.5$ nS

6 Discussion

One of the key observations from Tabak et al. (2011) was that the conductance and activation rate of BK current played vital roles in the spiking/bursting activity of pituitary cells. The aim to understand these observations motivated the study of a 4D multiple timescale pituitary cell model. Full system bifurcation analysis showed the sensitivity of the MMOs to both the activation time constant and conductance of the BK channels. Geometric singular perturbation theory was then used to formally decompose the system (Eq. (1)) into slow and fast subsystems, which provided the theoretical framework necessary to understand the burst generating mechanisms. For our model, there are various ways in which the system can be decomposed via GSPT. In this work we made the assumption that V and b are both fast variables operating on similar timescales. This led to the formal definition of the ratio of timescales r, which we assumed at the outset was $\mathcal{O}(1)$. A subtle issue with this approach is the fact that variations in τ_{BK} essentially alter the nature of the activation variable b: for small τ_{BK}, b is fast whilst for large τ_{BK}, b is slow. We remark here that the limit $r \to 0$ in the 2-fast/2-slow decomposition converges to the results of a 1-fast/2-slow decomposition with b constrained to its steady state function $b_\infty(V)$. Similarly, the limit $r \to \infty$ in the 2-fast/2-slow decomposition converges to the results of a 1-fast/3-slow decomposition with V fast and (n, b, c) slow. In either limit, there is only one fast variable and the system is restricted to generating canard-type MMOs. In any case, the 2-fast/2-slow approach encapsulates all of the information from the instantaneous BK approach and from the 1-fast/3-slow approach.

The central aim of this work has been to understand the role of BK conductance in the spiking/bursting activity of pituitary cells and why the BK activation rate also needed to be fast for a burst promoting effect. In the past, the burst promoting role of g_{BK} has been explained physiologically in the following way: g_{BK} turns on early during the spike, limiting spike amplitude, so g_K does not fully activate (which is reflected in Figs. 6 and 8 by the restricted range of n). Consequently, the membrane potential remains around a plateau until g_{SK} activates sufficiently to terminate the bursts. Using the 2-fast/2-slow splitting, we supplemented this classic explanation with a mathematical framework and showed that there are two distinct ways in which the MMOs can manifest in Eq. (1): via canard dynamics or slow passage through a dynamic Hopf bifurcation. In particular, we showed that the type of trajectory (canard-induced MMO, Hopf-induced MMO, spike or plateau oscillation) depended crucially on the interplay between the activation rate and maximal conductance of the BK current. We also demonstrated that τ_{BK} was a very useful diagnostic in distinguishing between canard- and Hopf-induced MMOs since τ_{BK} only appears in the fast subsystem (via the ratio r of fast timescales).

Using the eigenvalues of the layer problem as a diagnostic, we demonstrated that the slow passage effect provided the explanation for how trajectories could transition from spiking to bursting to plateauing under variations in the activation rate of the BK current. When g_{BK} is slowly activated (i.e. τ_{BK} or r large), the eigenvalues of Eq. (6) are complex over a very short interval in phase space. This gives the trajectories insufficient time to oscillate and the resulting pattern is a spike. When τ_{BK} is fast (r small), the region of complex eigenvalues of Eq. (6) occupies a larger region of phase space and provides the trajectories more time to oscillate before jumping away to the silent phase. For very fast activation time constants ($r \to 0$), the eigenvalues of Eq. (6) alternate from real to complex back to real. As such, any oscillatory behaviour quickly decays and a flat plateau is observed.

One of the hallmarks of the Hopf-induced MMOs is the sensitivity to variations in τ_{BK}. Two easily observable traits that change dramatically with τ_{BK} are the number and amplitude of small oscillations in the burst pattern. To test the model predictions, we blocked BK channels in GH4 cells and injected artificial BK current (via dynamic clamp) at different activation rates. We observed that at the onset of bursting, the amplitude of the sub-threshold oscillations is large. Injecting more rapidly activated BK current reliably decreased the amplitude of the small oscillations. For injected BK current with sufficiently fast activation time constant, the small oscillations essentially disappear and the bursting is replaced by plateau behaviour. Thus, the dynamic clamp experiments support the notion that the bursting arises from Hopf-induced MMOs. However, the Hopf mechanism alone is insufficient to explain all of the bursting behaviour. In particular, bursting in the absence of BK current can only be explained (within the confines of Eq. (1)) via canard dynamics.

We have demonstrated the potency of combining theory, numerics and experimentation. The theory of canard- and Hopf-induced mixed mode oscillations provides a theoretical framework in which experimental predictions can be made. The dynamic clamp technique can then be used to confirm or counter these predictions. In spite of the success of these techniques, there are various limitations and complications that have yet to be addressed. Most notable is the fact that the results of GSPT break down away from the singular limit. In the case of canard-induced MMOs, the bifurcation structure of Eq. (7) provides a good approximation to the bifurcation structure of Eq. (1) for sufficiently small perturbations (see Teka et al. 2011; Vo et al. 2010 for examples). No such comparison can be made between singular and non-singular bifurcation structures for the Hopf-induced MMOs. Further compounding the issue is the

question of how the switch from canard-induced MMOs to Hopf-induced MMOs occurs in the fully perturbed problem (1). In the singular limit, the switch can be well understood as a Bogdanov-Takens bifurcation of the layer problem, which alters the jumping mechanism for the singular orbits. How the switch in the oscillation mechanism perturbs (i.e. how the slow and fast subsystems interact away from the singular limit) is much less clear. Studies of how the BT bifurcation unfolds in systems with one slow variable have been considered (Golubitsky et al. 2001; Chiba 2011), however, our case is different since we have two slow variables and the canard phenomenon is generic. On the experimental side, we have provided evidence for the Hopf-induced MMOs but experimental evidence for the canard-induced MMOs is currently tenuous and is left to future work.

Acknowledgments TV was partially supported by an A.E. and F.A.Q. Stephens Scholarship and a Philipp Hofflin International Research Scholarship (University of Sydney). TV is also grateful to Florida State University for its hospitality, where this work was carried out. RB and JT were supported by NSF grant DMS 1220063. MW was partially supported by the Australian Research Council and the Marsden Fund, New Zealand.

Conflict of interest The authors declare that they have no competing interests.

References

Baer, S.M., Erneux, T., Rinzel, J. (1989). The slow passage through a Hopf bifurcation: delay, memory effects, and resonance. *SIAM Journal on Applied Mathematics*, *49*, 55–71.

Berglund, N., Gentz, B., Kuehn, C. (2012). Hunting french ducks in a noisy environment. *Journal of Differential Equations*, *252*, 4786–4841.

Bertram, R., & Sherman, A. (2005). Negative calcium feedback: the road from chay-keizer. In S. Coombes, & P. Bresslof (Eds.), *The genesis of rhythm in the nervous system* (pp. 19–48). New Jersey: World Scientific.

Bertram, R., Butte, M.J., Kiemel, T., Sherman, A. (1995). Topological and phenomenological classification of bursting oscillations. *Bulletin of Mathematical Biology*, *57*, 413–439.

Brøns, M., Krupa, M., Wechselberger, M. (2006). Mixed mode oscillations due to the generalized canard phenomenon. *Fields Institute Communications*, *49*, 39–63.

Brøns, M., Kaper, T.J., Rotstein, H.G. (2008). Introduction to focus issue: mixed mode oscillations: experiment, computation, and analysis. *Chaos*, *18*, 015–101.

Chiba, H. (2011). Periodic orbits and chaos in fast-slow systems with bogdanov-takens type fold points. *Journal of Differential Equations*, *250*, 112–160.

Del Negro, C.A., Hsiao, C.F., Chandler, S.H. (1999). Outward currents influencing bursting dynamics in guinea pig trigeminal motoneurons. *Journal of Neurophysiology*, *81*, 1478–1485.

Desroches, M., Guckenheimer, J., Krauskopf, B., Kuehn, C., Osinga, H.M., Wechselberger, M. (2012). Mixed-mode oscillations with multiple time scales. *SIAM Review*, *54*, 211–288.

Doedel, E.J. (1981). AUTO: a program for the automatic bifurcation analysis of autonomous systems. *Congressus Numerantum*, *30*, 265–284.

Doedel, E.J., Champneys, A.R., Fairgrieve, T.F., Kuznetsov, Y.A., Oldeman, K.E., Paffenroth, R.C., Sanstede, B., Wang, X.J., Zhang, C. (2009). AUTO-07P: continuation and bifurcation software for ordinary differential equations. Available from: http://cmvl.cs.concordia.ca/.

Dorodnitsyn, A.A. (1947). Asymptotic solution of the van der pol equation. *Proceedings of the Institute of Mechanics of the Academy of Science of the USSR XI*.

Erchova, I., & McGonigle, D.J. (2008). Rhythms of the brain: an examination of mixed mode oscillation approaches to the analysis of neurophysiological data. *Chaos*, *18*, 015–115.

Ermentrout, B., & Wechselberger, M. (2009). Canards, clusters, and synchronization in a weakly coupled interneuron model. *SIAM Journal of Applied Dynamical Systems*, *8*, 253–278.

Ermentrout, G.B., & Terman, D.H. (2010). *Mathematical Foundations of Neuroscience*: Springer.

Fakler, B., & Adelman, J.P. (2008). Control of K(Ca) channels by calcium nano/microdomains. *Neuron*, *59*, 873–881.

Fenichel, N. (1979). Geometric singular perturbation theory for ordinary differential equations. *Journal of Differential Equations*, *31*, 53–98.

Golubitsky, M., Josic, K., Kaper, T.J. (2001). An unfolding theory approach to bursting in fast-slow systems. In H.W. Broer, B. Krauskopf, G. Vegter (Eds.), *Global analysis of dynamical systems* (pp. 277–308). Bristol: Institute of Physics Publishing.

Grasman, J. (1987). *Asymptotic methods for relaxation oscillations and applications*. NY: Springer-Verlag.

Harvey, E., Kirk, V., Wechselberger, M., Sneyd, J. (2011). Multiple timescales, mixed mode oscillations and canards in models of intracellular calcium dynamics. *Journal of Nonlinear Science*, *21*, 639–683.

Izhikevich, E.M. (2000). Neural excitability, spiking and bursting. *International Journal of Bifurcation and Chaos*, *10*, 1171–1266.

Izhikevich, E.M. (2007). *Dynamical Systems in Neuroscience: The Geometry of Excitability and Bursting*. Cambridge: The MIT Press.

Jones, C.K.R.T. (1995). Geometric singular perturbation theory. In R. Johnson (Ed.), *Dynamical systems. Lecture notes in mathematics* (Vol. 1609, pp. 44–120). New York: Springer.

Kuehn, C. (2011). A mathematical framework for critical transitions: bifurcations, fast-slow systems and stochastic dynamics. *Physica D*, *240*, 1020–1035.

Latorre, R., & Brauchi, S. (2006). Large conductance Ca^{2+}-activated K^+ (BK) channel: activation by Ca^{2+} and voltage. *Biological Research*, *39*, 385–401.

LeBeau, A.P., Robson, A.B., McKinnon, A.E., Sneyd, J. (1998). Analysis of a reduced model of corticotroph action potentials. *Journal of Theoretical Biology*, *192*, 319–339.

Miranda, P., de la Peña, P., Gómez-Varela, D., Barros, F. (2003). Role of BK potassium channels shaping action potentials and the associated Ca_i^{2+} oscillations in GH_3 rat anterior pituitary cells. *Neuroendocrinology*, *77*, 162–176.

Mishchenko, E.F., & Rozov, N.K. (1980). *Differential equations with small parameters and relaxation oscillations*. Plenum (Translated from Russian).

Mishchenko, E.F., Kolesov, Y.S., Kolesov, A.Y., Rhozov, N.K. (1994). Asymptotic methods in singularly perturbed systems. Monographs in contemporary mathematics. New York: Consultants Bureau.

Neishtadt, A.I. (1987). Persistence of stability loss for dynamical bifurcations. I. *Differential Equations*, *23*, 1385–1391.

Neishtadt, A.I. (1988). Persistence of stability loss for dynamical bifurcations. II. *Differential Equations*, *24*, 171–176.

Nowacki, J., Mazlan, S., Osinga, H.M., Tsaneva-Atanasova, K. (2010). The role of large-conductance calcium-activated K^+ (BK) channels in shaping bursting oscillations of a somatotroph cell model. *Physica D*, *239*, 485–493.

Osinga, H.M., & Tsaneva-Atanasova, K. (2010). Dynamics of plateau bursting depending on the location of its equilibrium. *Journal of Neuroendocrinology*, *22*, 1301–1314.

Rinzel, J. (1985). Bursting oscillations in an excitable membrane model. In *Lecture notes in mathematics* (Vol. 1151, pp. 304–316).

Rotstein, H., Wechselberger, M., Kopell, N. (2008). Canard induced mixed-mode oscillations in a medial entorhinal cortex layer II stellate cell model. *SIAM Journal of Applied Dynamical Systems*, *7*, 1582–1611.

Rubin, J., & Terman, D. (2002). Geometric singular perturbation analysis of neuronal dynamics. In B. Fiedler (Ed.), *Handbook of dynamical systems* (Vol. 2, pp. 93–146). Elsevier.

Rubin, J., & Wechselberger, M. (2008). The selection of mixed-mode oscillations in a Hodgkin-Huxley model with multiple timescales. *Chaos*, *18*, 015–105.

Safiulina, V.F., Zacchi, P., Taglialatela, M., Yaari, Y., Cherubini, E. (2008). Low expression of kv7/m channels facilitates intrinsic and network bursting in the developing rat hippocampus. *Journal of Physiology*, *586*, 5437–5453.

Sah, P., & Faber, E.S. (2002). Channels underlying neuronal calcium-activated potassium currents. *Progress in Neurobiology*, *66*, 345–353.

Sharp, A.A., Neil, M.B.O., Abbott, L.F., Marder, E. (1993). Dynamic clamp – computer-generated conductances in real neurons. *Journal of Neurophysiology*, *69*, 992–995.

Sherman, A., Keizer, J., Rinzel, J. (1990). Domain model for Ca^{2+}-inactivation of Ca^{2+} channels at low channel density. *Biophysical Journal*, *58*, 985–995.

Stern, J.V., Osinga, H.M., LeBeau, A., Sherman, A. (2008). Resetting behavior in a model of bursting in secretory pituitary cells: distinguishing plateaus from pseudo-plateaus. *Bulletin of Mathematical Biology*, *70*, 68–88.

Stojilkovic, S.S., Zemkova, H., Goor, F.V. (2005). Biophysical basis of pituitary cell type-specific Ca^{2+} signaling-secretion coupling. *Trends In Endocrinology and Metabolism*, *16*, 152–159.

Stojilkovic, S.S., Tabak, J., Bertram, R. (2010). Ion channels and signaling in the pituitary gland. *Endocrine Reviews*, *31*, 845–915.

Szmolyan, P., & Wechselberger, M. (2004). Relaxation oscillations in $\mathbb{R}^3$. *Journal of Differential Equations*, *200*, 69–104.

Tabak, J., Tomaiuolo, M., Gonzalez-Iglesias, A.E., Milescu, L.S., Bertram, R. (2011). Fast-activating voltage- and calcium-dependent potassium (BK) conductance promotes bursting in pituitary cells: a dynamic clamp study. *Journal of Neuroscience*, *31*, 16,855–16,863.

Teka, W., Tabak, J., Vo, T., Wechselberger, M., Bertram, R. (2011). The dynamics underlying pseudo-plateau bursting in a pituitary cell model. *Journal of Mathematical Neuroscience*, *1*(12).

Teka, W., Tsaneva-Atanasova, K., Bertram, R., Tabak, J. (2011). From plateau to pseudo-plateau bursting: Making the transition. *Bulletin of Mathematical Biology*, *73*, 1292–1311.

Terman, D. (1991). Chaotic spikes arising from a model of bursting in excitable membranes. *SIAM Journal on Applied Mathematics*, *51*, 1418–1450.

Tsaneva-Atanasova, K., Sherman, A., Goor, F.V., Stojilkovic, S.S. (2007). Mechanism of spontaneous and receptor-controlled electrical activity in pituitary somatotrophs: experiments and theory. *Journal of Neurophysiology*, *98*, 131–144.

Tsaneva-Atanasova, K., Osinga, H.M., Rieb, T., Sherman, A. (2010). Full system bifurcation analysis of endocrine bursting models. *Journal of Theoretical Biology*, *264*, 1133–1146.

Van Goor, F., Zivadinovic, D., Martinez-Fuentes, A.J., Stojilkovic, S.S. (2001). Dependence of pituitary hormone secretion on the pattern of spontaneous voltage-gated calcium influx. Cell-type specific action potential secretion coupling. *Journal of Biological Chemistry*, *276*, 33,840–33,846.

Vo, T., Bertram, R., Tabak, J., Wechselberger, M. (2010). Mixed mode oscillations as a mechanism for pseudo-plateau bursting. *Journal of Computational Neuroscience*, *28*, 443–458.

Vo, T., Bertram, R., Wechselberger, M. (2012). Multiple geometric viewpoints of mixed mode dynamics. *SIAM Journal of Applied Dynamical Systems*, *12*, 789–830.

Wechselberger, M. (2005). Existence and bifurcation of canards in $\mathbb{R}^3$ in the case of a folded node. *SIAM Journal of Dynamic Systems*, *4*, 101–139.

Wechselberger, M. (2012). Apropos canards. *Transactions of the American Mathematical Society*, *364*, 3289–3309.

Wechselberger, M., & Weckesser, W. (2009). Bifurcations of mixed-mode oscillations in a stellate cell model. *Physica D*, *238*, 1598–1614.